

Accepted Manuscript

Petrogenesis of shield volcanism from the Juan Fernández Ridge, Southeast Pacific: Melting of a low-temperature pyroxenite-bearing mantle plume

Javier Reyes, Luis E. Lara, Folkmar Hauff, Kaj Hoernle, Diego Morata, Daniel Selles, Oliver Cooper

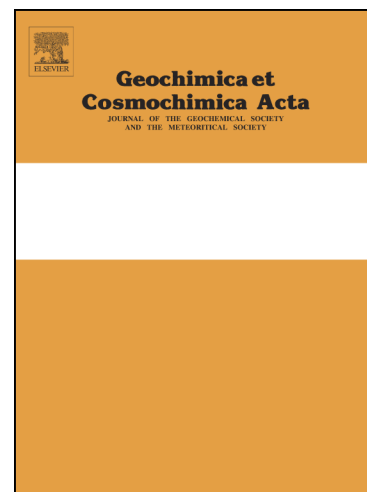
PII: S0016-7037(19)30261-3
DOI: <https://doi.org/10.1016/j.gca.2019.05.004>
Reference: GCA 11230

To appear in: *Geochimica et Cosmochimica Acta*

Received Date: 10 May 2018
Revised Date: 3 May 2019
Accepted Date: 3 May 2019

Please cite this article as: Reyes, J., Lara, L.E., Hauff, F., Hoernle, K., Morata, D., Selles, D., Cooper, O., Petrogenesis of shield volcanism from the Juan Fernández Ridge, Southeast Pacific: Melting of a low-temperature pyroxenite-bearing mantle plume, *Geochimica et Cosmochimica Acta* (2019), doi: <https://doi.org/10.1016/j.gca.2019.05.004>

This is a PDF file of an unedited manuscript that has been accepted for publication. As a service to our customers we are providing this early version of the manuscript. The manuscript will undergo copyediting, typesetting, and review of the resulting proof before it is published in its final form. Please note that during the production process errors may be discovered which could affect the content, and all legal disclaimers that apply to the journal pertain.



**Petrogenesis of shield volcanism from the Juan Fernández Ridge,
Southeast Pacific: Melting of a low-temperature pyroxenite-bearing
mantle plume**

Javier Reyes ^{1,2,8*}, **Luis E. Lara** ^{3, 4}, **Folkmar Hauff** ⁵, **Kaj Hoernle** ^{5,6}, **Diego Morata** ^{1,2},
Daniel Selles ^{7,9}, **Oliver Cooper** ¹

¹ Departamento de Geología, Facultad de Ciencias Físicas y Matemáticas, Universidad de Chile, Santiago, Chile

² Centro de Excelencia en Geotermia de Los Andes, Santiago, Chile

³ Volcano Hazards Program, Servicio Nacional de Geología y Minería, Santiago, Chile

⁴ Research Center for Integrated Disaster Risk Management (CIGIDEN), Santiago, Chile

⁵ GEOMAR Helmholtz-Zentrum für Ozeanforschung Kiel, Kiel, Germany

⁶ Institut für Geowissenschaften, Christian-Albrechts Universität zu Kiel, Kiel, Germany

⁷ Aurum Consultores, Santiago, Chile

⁸ Escuela de Geología, Facultad de Ciencias, Universidad Mayor

⁹ Teck Resources Chile Ltda.

* Corresponding autor

E-mail address: jareyes@ing.uchile.cl; javier.reyes@umayor.cl (J. Reyes)

Abstract

The Juan Fernández Ridge (JFR) is an age-progressive volcanic chain (~800 km long) related to a fixed mantle plume in the Southeast Pacific offshore central Chile. The high $^3\text{He}/^4\text{He}$ ratio (up to 18 times higher than that of the atmosphere) and spatiotemporal $^{40}\text{Ar}/^{39}\text{Ar}$ geochronology suggest that the source material of the JFR is derived from the lower mantle and transferred to the surface by a relatively stationary plume. We used new whole-rock geochemical data (major-element, trace-element, and Sr–Nd–Pb isotopic data) for representative samples from the shield-stage of volcanism in the JFR (from O'Higgins Guyot, Alpha Seamount, Robinson Crusoe Island, and Alejandro Selkirk Island) to develop a petrogenetic model with the goal of understanding the temporal and spatial evolution of magmatism along the JFR. The shield-building lavas of JFR consist primarily of tholeiitic to alkalic basalts. Their compositional differences are explained by the fractional crystallization of olivine and clinopyroxene \pm plagioclase, magmatic recharge, melt mixing, and olivine accumulation. Radiogenic Sr–Nd–Pb isotopes show a narrow field within the compositional range of the common FOZO mantle. The $^{206}\text{Pb}/^{204}\text{Pb}$ and $^{207}\text{Pb}/^{204}\text{Pb}$ ratios of JFR lavas are similar to those of other islands on the Nazca Plate (e.g., San Félix and San Ambrosio). However, the JFR lavas are more radiogenic and show a narrower compositional range compared to the Easter Seamount Chain. The low CaO content at a given MgO content, moderate Ti–Ta–Nb 'TITAN' anomaly, fractionated heavy rare earth element values, and isotopic composition of JFR lavas are consistent with the presence of pyroxenite (recycled oceanic crust) in the mantle source. To estimate source parameters, we used OBS1 software (Kimura and Kawabata, 2015) to calculate the potential temperature (1316°C–1412°C), total degree of melting (3.4–19.2 wt%), and pyroxenite fraction (0.6–18.4 wt%) of the mantle beneath JFR. The temporal changes in the thermal, compositional, and lithologic characteristics of the source material can explain the chemical differences observed between different JFR volcanoes. We propose that shield-stage volcanism in JFR is largely generated by the melting of pyroxenite in a relatively low-

temperature mantle plume. As a result, this weak plume containing low mantle He is difficult to image using seismic tomography.

1. Introduction

Age-progressive oceanic intraplate magmatism is characterized by the formation of large basaltic shield volcanoes that form volcanic chains of islands and seamounts on oceanic crust. The movement of the plate above a relatively fixed mantle upwelling (plume) is the most accepted theory to explain age-progressive oceanic intraplate magmatism (the so-called 'hotspot hypothesis') (e.g., Morgan, 1971; Morgan, 1972). However, a number of volcanic alignments do not show age progression, as pointed out by Clouard and Bonneville (2001) for the Pacific Ocean basin. Alternative models have been proposed, such as non-fixed plumes (Steinberger and O'Connell, 1988) and tectonically controlled decompression melting related to magmatic hydrofracture driven by flexural stresses in the presence of a volcanic load (Hieronymus and Bercovici, 2000). More frequent processes including subduction cooling, continental insulation, and small-scale convection beneath ridges, rifts, and fracture zones (Anderson, 2000, 2001); delamination during continental breakup and subsequent upwelling beneath mid-ocean ridges (Hoernle et al., 2011); and small-scale sublithospheric convection (Ballmer et al., 2007) could also potentially explain intraplate volcanism on oceanic plates.

The diverse elemental and isotopic compositions of mid-ocean ridges and intraplate volcanism around the globe suggest that the underlying mantle is heterogeneous in terms of mineralogy, lithology, and composition (Zindler and Hart, 1986 and references therein).

The classical end-member compositions involved in ocean island basalt (OIB) genesis are: depleted "MORB-source" mantle (DM) and other end-members formed by the recycling of various crustal materials; high μ (HIMU), where $\mu = {}^{238}\text{U}/{}^{204}\text{Pb}$ (e.g., Zindler and Hart,

1986; Weaver, 1991; Hauri and Hart, 1993; Salters and White, 1998; Stracke et al., 2003 and 2005; Kimura et al., 2016; Homrighausen et al., 2018a, 2018b); and enriched mantle one (EM1) and two (EM2) (e.g., Othman et al., 1984; Blichert-Toft et al., 1999; Geldmacher et al., 2008; Willbold and Stracke, 2010; Hoernle et al., 2011; Kimura et al., 2016; Turner et al., 2017). Additionally, a common component recognized in some OIBs is referred to as prevalent mantle (PREMA) (Zindler and Hart, 1986), common component (C) (Hanan and Graham, 1996), or Focal Zone (FOZO) (Hart et al., 1992). In this paper, we use the term FOZO. Herein, FOZO is interpreted as a relatively uniform mixture of other components or may reflect the chemical heterogeneity in recycled oceanic crust (e.g., Stracke et al., 2005; White, 2015; Kimura et al., 2016). Based on the geochemistry of OIBs worldwide, the existence of recycled lithologies, particularly igneous oceanic crust as pyroxenite in the OIB source, is highly likely (e.g., Hofmann and White, 1982; Hofmann, 1988; Herzberg, 2006; Sobolev et al., 2007).

The Juan Fernández Ridge (JFR) is a poorly investigated intraplate volcanic chain. JFR is an aseismic ridge that contains approximately 15 volcanoes (two main islands and at least 12 seamounts) and is emplaced on the Nazca Plate in the Southeast Pacific, which is being subducted beneath the South American Plate margin at $\sim 33.4^{\circ}\text{S}$ (Figure 1). The age of the crust in this area is ca. 27–32 Ma (Lara et al., 2018b and references therein). JFR was early interpreted as an expression of a mantle plume (Farley et al., 1993; Devey et al., 2000). In the hotspot catalogue of Courtillot et al. (2003), JFR satisfies three out of the five criteria for originating from a primary mantle plume. These criteria include a relatively high buoyancy flux of $1.6\text{--}1.7 \text{ Mg}\cdot\text{s}^{-1}$ (Davies, 1988; Sleep, 1990) and a high $^3\text{He}/^4\text{He}$ value (7.8–18) compared to the atmospheric ratio (R_A) (Farley et al., 1993; Jackson et al., 2017; Truong et al., 2018). New detailed $^{40}\text{Ar}/^{39}\text{Ar}$ age dating (Lara et al., 2018b) demonstrates the presence of a clear east-to-west age progression for the shield-stage of at least four

volcanoes in JFR, consistent with previous imprecise K–Ar (Booker et al., 1967; Stuessy et al., 1984; von Huene et al., 1997) and some recent $^{40}\text{Ar}/^{39}\text{Ar}$ ages (Reyes et al., 2017; Lara et al., 2018a). The interpretation of seismic tomographic data beneath JFR have led to opposing conclusions. While Montelli et al. (2006) proposed a plume derived from intermediate depth, Boschi et al. (2007) did not recognize a plume. More recently, French and Romanowicz (2015) imaged a vertical conduit beneath the JFR; however, it is not clearly continuous.

JFR is isolated from two active spreading ridges, the East Pacific Rise (EPR; ~2500 km to the west) and Chile Rise (>850 km to the south; Figure 1). This provides an opportunity to (1) study the source composition of intraplate volcanism beneath the Southeast Pacific, (2) compare it with other instances of intraplate volcanism worldwide, and (3) assess the possible chemical influence of the subducted JFR on Andean magmatism. In this contribution, we report new geochemical data (major-element, trace-element, and Sr–Nd–Pb isotope data) corresponding to shield-stage magmatism in JFR with the goal of understanding its petrogenesis and magmatic evolution. We then use the OBS1 model (Kimura and Kawabata, 2015) to determine the plausible physical and chemical conditions of the mantle source.

2. Geologic background

JFR comprises two main islands and at least 12 seamounts with a common base at ca. 3900 meters below sea level (m b.s.l.) (Rodrigo and Lara, 2014). This study focuses primarily on four volcanic centers where shield volcanism has been recognized: O'Higgins Guyot, Alpha Seamount, Robinson Crusoe Island, and Alejandro Selkirk Island (from east to west; Figure 1). O'Higgins Guyot is a volcanic shield edifice that is ca. 3450 m higher than the seafloor and has a flat top that is ca. 500 m b.s.l. on average. A sequence of fresh

rejuvenated (or post-erosional) lavas dip gently southward from a vent at ca. 360 m b.s.l. and overlie the flat surface on the shield lavas of the guyot (Lara et al., 2018a).

The Alpha Seamount, which lies approximately 450 km to the west of O'Higgins Guyot, has a summit at 260–450 m b.s.l. (Farley et al., 1993). The chemical similarities, including whole-rock geochemistry and isotopic signatures (see Farley et al., 1993 and Section 4 of this paper), between samples from Alpha Seamount and other JFR shield lavas suggest that Alpha Seamount is also at the shield-stage of volcanism. Robinson Crusoe Island (height = 915 m) is located approximately 20 km west of Alpha Seamount. The nearby Santa Clara Island (height = 375 m) is hereafter considered to be part of Robinson Crusoe Island because their grounds are on the same volcanic pedestal. These islands are the main volcanic edifices on JFR. Deep coastal erosion has exposed thick sequences representative of the upper shield-stage sequence (Baker et al., 1987; Farley et al., 1993; Reyes et al., 2017), and a sharp erosional unconformity separates the shield-stage sequence from the upper alkaline rejuvenated-stage (Reyes et al., 2017). Alejandro Selkirk Island (height = 1320 m) is another emerged volcanic edifice located approximately 180 km west of Robinson Crusoe Island. Alejandro Selkirk Island is an asymmetric shield remnant with long straight valleys on its eastern slope and high cliffs on its western side. Our samples from late shield-stage volcanism came primarily from the upper slopes of O'Higgins Guyot and Alpha Seamount along with the subaerial sections of the Alejandro Selkirk and Robinson Crusoe islands.

The shield-stage lavas from O'Higgins Guyot, Alpha Seamount, Robinson Crusoe Island, and Alejandro Selkirk Island produced $^{40}\text{Ar}/^{39}\text{Ar}$ ages of 8.41–9.26 Ma (von Huene et al., 1997; Lara et al., 2018a), 4.58–4.63 Ma (Lara et al., 2018b), 3.40–4.10 Ma (Reyes et al., 2017; Lara et al., 2018b), and 0.83–0.94 Ma (Lara et al., 2018b), respectively. The progressively younger $^{40}\text{Ar}/^{39}\text{Ar}$ ages moving westward are partially consistent with the

eastward Nazca Plate movement of ~ 70.5 mm/yr (GEODVEL 2010 model; Argus et al., 2010) supporting the mantle plume hypothesis, although some westward shift is inferred (Lara et al., 2018b). In addition to shield volcanism, rejuvenated magmatism has been reported for Robinson Crusoe Island (Reyes et al., 2017) and for the summit of O'Higgins Guyot (Lara et al., 2018a); however, the nature of these rocks is beyond the scope of this study.

Lavas from the shield-stage of JFR are mainly alkaline and subalkaline basalts and picrites that are enriched in large-ion lithophile elements (LILEs) and high-field-strength elements (HFSEs), which is typical of OIBs (e.g., Baker et al., 1987; Reyes et al., 2017; Lara et al., 2018a). The Sr–Nd–Pb isotopic values of these lavas show a DUPAL signature (Gerlach et al., 1986) and a FOZO component (Jackson et al., 2007), with slight compositional differences between volcanic centers.

An important feature of some JFR lavas is a high $^3\text{He}/^4\text{He}$ ratio. However, there is no correlation between He and Sr–Nd–Pb isotopes. The Robinson Crusoe shield lavas show the highest values of $^3\text{He}/^4\text{He}$ in JFR (13.6–18 R_A), followed by the rejuvenated-stage on the same island (11.2–12.5 R_A) and the shield-stage of Alejandro Selkirk Island (7.8–9.5 R_A) (Farley et al., 1993). The high $^3\text{He}/^4\text{He}$ ratio in shield-stage lavas was attributed to a FOZO-type component in the source of these lavas. In addition, the relative low $^3\text{He}/^4\text{He}$ ratio in Alejandro Selkirk Island suggests the involvement of a depleted component in their origin (Truong et al., 2018). A HIMU component was also proposed to be involved in the genesis of JFR, particularly in Domingo and Friday seamounts, two volcanic edifices located approximately 80–100 km west of Alejandro Selkirk Island that likely represent the early or pre-shield stages of JFR volcanism (Devey et al., 2000). From a more regional point of view, Gerlach et al. (1986) recognized differences in JFR compared to other

oceanic islands far from spreading ridges in the Nazca Plate (San Félix and San Ambrosio), which might indicate that these islands were derived from distinct sources.

3. Sampling and analytical procedures

Six samples from O'Higgins Guyot were dredged during the SO101 CONDOR cruise of the German RV Sonne in 1995 (more details and data in Lara et al., 2018a). Ten samples of dredged rocks from Alpha Seamount were provided by the Scripps Institution of Oceanography (University of California, San Diego, USA), and two additional samples were provided by Hernán Vergara; all 12 were collected during the HYDROS Expedition (Leg I) in 1988 (HYDR01MV) on RV Melville (USA). One additional sample was collected in 2016 with a biological dredge during the CIMAR 22 cruise on board the Chilean AGS61 Cabo de Hornos vessel. Seventy-nine lava and dyke samples (48 from Robinson Crusoe Island and 31 from Alejandro Selkirk Island) were collected during several field campaigns between 2011 and 2013. We preferred samples with a low degree of alteration and low abundance of vesicles. From the Scripps Institution of Oceanography, we also received six subaerial samples from Alejandro Selkirk Island collected during the 1988 HYDR01MV expedition. Representative samples were analyzed by optical microscopy to reveal their petrographic characteristics. Some samples were also investigated by scanning electron microscopy (FEI Quanta 250) at the Centro de Excelencia en Geotermia de Los Andes facilities of Universidad de Chile. Digital modal counts (500 points, recursive grid) were performed on 26 samples (Table 1) using JMicroVision 1.2.7 software.

Whole-rock major and trace elements were analyzed at Acme Labs (Vancouver, Canada) at different times but following the same procedure. Rock chips produced by crushing field hand samples were pulverized to 85% and passed through a 200-mesh (< 0.074 mm) sieve. Separated aliquots were then fused with lithium metaborate/tetraborate for major-

element analysis by inductively coupled plasma-emission spectroscopy and digested with dilute nitric acid for trace-element analysis using inductively coupled plasma-mass spectrometry (ICP-MS). A separate split was digested in aqua regia and analyzed by ICP-MS to determine the Ni and Pb contents. Loss on ignition (LOI) was determined after sample powder ignition at 1000°C. Based on repeated analyses of ACME internal standards (mainly SO-18, details in Table S.1) and duplicated samples (Table S.2), the accuracy (relative deviations between measured standards and their reference values) and analytical precision (estimated from sample replicates) were typically better than 2% and 1%, respectively, except for P₂O₅ (< 4.5% and < 2.3%, respectively). For trace elements, both values were <10%, except for Pb (measured values very close to the detection limit). The detection limits varied from 0.01 to 0.04 wt% for major elements and from 0.01 to 1 ppm for trace elements (details in Tables 2 and 3). The values measured for blank samples were typically under the detection limits for all major and trace elements.

Sr–Nd–Pb isotope ratios were determined on rock chips for 15 samples, with two replicates for each sample. Detailed descriptions of sample preparation and the procedures used for chemical analysis and mass spectrometry can be found in Hoernle et al. (2008). Briefly, Sr, Nd, and Pb isotope ratios were determined by thermal ionization mass spectrometry (TIMS) at GEOMAR Helmholtz Centre (Kiel, Germany) using a Thermo Fisher Scientific TRITON+ instrument for Sr and Nd isotopic measurements and a TRITON+ and Finnigan MAT 262-RPQ2+ instrument for Pb isotopic measurements. Prior to acid digestion, rock chips (100–150 mg of the 0.5–2-mm fraction) were leached in 2 N HCl at 70°C for 1–2 h and then rinsed three times with 18.2-MΩ water to remove possible alteration phases such as carbonates. All reported errors are at the 2σ confidence level. Strontium and Nd isotope ratios were mass bias corrected using within-run values of 0.1194 for ⁸⁶Sr/⁸⁸Sr and 0.7219 for ¹⁴⁶Nd/¹⁴⁴Nd. The measured ⁸⁷Sr/⁸⁶Sr value for the

NBS987 reference material was 0.710264 ± 0.000009 [two standard deviations (2SD); $n = 102$], while the $^{143}\text{Nd}/^{144}\text{Nd}$ value for the La Jolla reference material was 0.511843 ± 0.000006 (2SD; $n = 114$). Sample data are reported relative to $^{87}\text{Sr}/^{86}\text{Sr} = 0.710250$ for NBS987 and $^{143}\text{Nd}/^{144}\text{Nd} = 0.511850$ for La Jolla. The Pb double-spike (DS) technique of Hoernle et al. (2011) was used for the mass bias correction of Pb isotope ratios. The DS-corrected NBS981 values were $^{206}\text{Pb}/^{204}\text{Pb} = 16.9412 \pm 12$, $^{207}\text{Pb}/^{204}\text{Pb} = 15.4983 \pm 13$, $^{208}\text{Pb}/^{204}\text{Pb} = 36.7208 \pm 31$, $^{207}\text{Pb}/^{206}\text{Pb} = 0.914832 \pm 27$, and $^{208}\text{Pb}/^{206}\text{Pb} = 2.167549 \pm 82$ ($n = 22$) on the TRITON+ and $^{206}\text{Pb}/^{204}\text{Pb} = 16.9427 \pm 21$, $^{207}\text{Pb}/^{204}\text{Pb} = 15.5005 \pm 21$, $^{208}\text{Pb}/^{204}\text{Pb} = 36.7278 \pm 46$, $^{207}\text{Pb}/^{206}\text{Pb} = 0.914877 \pm 32$, and $^{208}\text{Pb}/^{206}\text{Pb} = 2.167765 \pm 63$ ($n = 17$) on the MAT262 instrument. These NBS981 ratios overlap within 2SD for each instrument and compare well with published DS and triple-spike (TS) data for NBS981 (see Hoernle et al., 2011). The analysis of unleached BHVO-2 ($n = 3$) during the same period gave $^{87}\text{Sr}/^{86}\text{Sr} = 0.703473 \pm 16$; $^{143}\text{Nd}/^{144}\text{Nd} = 0.512978 \pm 3$; $^{206}\text{Pb}/^{204}\text{Pb} = 18.651 \pm 41$; $^{207}\text{Pb}/^{204}\text{Pb} = 15.539 \pm 10$; and $^{208}\text{Pb}/^{204}\text{Pb} = 38.256 \pm 67$. These values compare well with the reference values of Jochum et al. (2016) ($^{87}\text{Sr}/^{86}\text{Sr} = 0.703478 \pm 34$ and $^{143}\text{Nd}/^{144}\text{Nd} = 0.512979 \pm 14$) and Baker et al. (2004) ($^{206}\text{Pb}/^{204}\text{Pb} = 18.649 \pm 19$, $^{207}\text{Pb}/^{204}\text{Pb} = 15.540 \pm 15$, and $^{208}\text{Pb}/^{204}\text{Pb} = 38.249 \pm 22$). Both series of USGS standards have been shown to be contaminated with Pb during powder preparation (e.g. Baker et al., 2004; Nobre Sivia et al., 2009; Todd et al., 2015). Therefore, Pb isotope analysis of these materials does not reproduce at similar levels as NBS981 or sample replicate analysis.

Sample analyses were replicated within 2SD of the NBS987, NBS981, and La Jolla references. Chemistry blanks were monitored for each batch of samples, and the amounts of Sr, Nd, and Pb were typically <100 pg (i.e., negligible compared to the amount of sample).

Eleven samples were analyzed for Sr–Nd isotopes by TIMS at the Laboratoire Magmas and Volcans isotope laboratory (Clermont-Ferrand, France) using a Thermo Fisher Triton instrument. The Sr and Nd isotopes were corrected for mass fractionation by normalization to $^{86}\text{Sr}/^{88}\text{Sr} = 0.1194$ and $^{146}\text{Nd}/^{144}\text{Nd} = 0.7219$, respectively. Strontium–Nd sample decomposition and chemical separation followed the procedure developed by Pin and Zalduegui (1997). The international standards NBS987 and JNd-1 gave $^{87}\text{Sr}/^{86}\text{Sr}$ and $^{143}\text{Nd}/^{144}\text{Nd}$ values of 0.710241 ± 6 (2SD) and 0.512102 ± 4 , respectively, during the analysis period. These values are within the range of error of the accepted standard values. Four samples were analyzed for Sr–Nd isotopes in both laboratories, with variations less than 0.000015 for $^{87}\text{Sr}/^{86}\text{Sr}$ (except for one sample, LL250711-5, with a difference of 0.000050) and less than 0.000009 for $^{143}\text{Nd}/^{144}\text{Nd}$.

4. Results

Due to their petrographic, geochemical, and isotopic similarities, the dyke samples from Robinson Crusoe and Alejandro Selkirk Islands are hereafter considered to be part of the shield-building stage and are consequently referred to as simply lavas. Based on the geochemical and mineralogical characteristics, Reyes et al. (2017) defined the following compositional groups for the shield-stage of Robinson Crusoe Island: (1) ‘differentiated’ [$\text{Mg\#} = \text{Mg}^{2+}/(\text{Mg}^{2+} + \text{Fe}^{2+}) < 58$, assuming 90% of total iron is ferrous iron in all samples, a reasonable estimate used for other oceanic islands such as Hawaii, e.g., García, 1996]; (2) ‘near-primitive’ ($58 < \text{Mg\#} < 68$; a lava that has undergone minimal differentiation); and (3) ‘olivine-rich’ ($\text{Mg\#} > 68$, primitive rocks in few cases, generally cumulates). These groups apply to the entire JFR shield sample set. For instance, O’Higgins Guyot has compositions that mimic those of the ‘differentiated’ and ‘olivine-rich’ groups, while the basalts of Alpha Seamount belong exclusively to the ‘differentiated’ lava group. Most samples from Robinson Crusoe and Alejandro Selkirk Islands fall within the ‘differentiated’

and 'olivine-rich' groups, although some also fall in the 'near-primitive' group (Figure 2). The boundary between the 'near-primitive' and 'olivine-rich' groups is diffuse, and some samples could be considered as part of both groups.

4.1 Petrography

The JFR shield-stage is commonly characterized by vesicular lavas (up to ~18 vol%; Table 1) ranging from porphyritic to aphanitic (highly vesicular lavas were not considered). The mineral components consist mainly of olivine, clinopyroxene, and plagioclase embedded in an intersertal to intergranular groundmass (subophitic in some basalts and picrites from the 'olivine-rich' group). Olivine is the main mineral phase in JFR, and phenocryst content reaches 5% in basalts from the 'differentiated' group, 13% in the 'near-primitive' group, and 47% in picrites from the 'olivine-rich' group (common values in this set are around 25%; Table 1). Clinopyroxene and plagioclase phenocrysts are in low abundance (commonly < 3%) or are absent in many samples, with a maximum content of 10% for clinopyroxene and 21% for plagioclase (both in the 'differentiated' group; Table 1). Opaque minerals such as Cr-rich spinel are visible mostly as inclusions in olivines of the 'olivine-rich' group. The groundmass has the same mineralogy but in different proportions; clinopyroxene and plagioclase are the most abundant phases followed by Fe–Ti oxides (mainly ilmenite and titanomagnetite) and scarce olivine. Submarine samples have a significant content of secondary minerals (mainly opaques and clays) in the groundmass, and iddingsite generally replaces at least some of the olivine crystals. In subaerial rocks, the content of secondary minerals is considerably lower (e.g., iddingsite rims of variable width in olivine crystals). In a few samples, vesicles are partially filled by clay minerals such as smectite. Some lavas recovered at the southwest coast of Robinson Crusoe Island are strongly altered and contain smectite, chlorite, calcite, and epidote; these lavas were not considered in this study.

4.2 Major element and Ni geochemistry

The SiO_2 contents and Mg# values of the JFR shield-building lavas ranged from 43.6–50.5 wt% and 42.2–80.3, respectively (Table 2). Please note that Table 2 presents the measured values of all major elements, while the data reported in the text and figures have been recalculated to total 100% on a LOI-free basis. Figure S.1 demonstrates that Na and K correlate well with incompatible elements like Nb (few samples showed mobilization of Na and K), allowing us to use the total alkali silica (TAS) classification diagram. According to the TAS (Figure 3), most samples are subalkaline (tholeiitic in accordance with the AFM diagram), transitional, or alkali basalts with subordinate trachy- and picro-basalts (picrites due to their high olivine, Mg, and Ti contents) (Table 1). Only two samples are classified as basanites and one as andesitic trachy-basalt; however, all three of these samples lie very close to the fields of the more abundant lithologies. The Ni contents vary from 18 to 1299 ppm (Figure 2) and show a curvilinear correlation with Mg#, allowing all the JFR shield lavas to be classified into the previously mentioned compositional groups ('differentiated,' 'near-primitive,' and 'olivine-rich') defined by Reyes et al. (2017) for Robinson Crusoe Island. Submarine samples from O'Higgins Guyot and Alpha Seamount are transitional and alkali basalts. However, for Robinson Crusoe Island and especially Alejandro Selkirk Island, the proportion of tholeiitic basalts is significant. All the islands/seamounts have major-element characteristics typical of OIBs (i.e., high TiO_2 and K_2O contents relative to MORB) (Pearce and Parkinson, 1993) and considerable variation can be observed in some elements as TiO_2 and $\text{Fe}_2\text{O}_3^{\text{T}}$, with a slight depletion at a given Mg# in the Alejandro Selkirk lavas (Table 2). Alpha Seamount lavas show enrichment in Al_2O_3 , Na_2O , K_2O (highly variable in all volcanoes), and P_2O_5 (Table 2 and Figure S.2), possibly due to low-temperature alteration.

4.3 Trace-element geochemistry

JFR shield-stage lavas show a marked enrichment in incompatible trace elements relative to MORB, including LILEs and HFSEs. Incompatible elements have negative correlations with Mg# and positive correlations with SiO₂. The ranges of LILE contents are similar for all volcanoes (e.g., 181–966 ppm Sr for all JFR) (Figure 2 and Table 3), with low minimum values in the O'Higgins and Alpha lavas. All JFR shield lavas and particularly the Robinson Crusoe lavas show moderately high values of Ti and, most notably, Ta and Nb (represented as Ti/Ti*, Nb/Nb*, and Ta/Ta*, respectively, in Figure 4). These features are considered as 'TITAN' anomalies and have generated interest as a unique feature of OIB magmas (Jackson et al., 2008). JFR shield lavas have La/Yb, La/Sm, and Gd/Yb ratios ranging from 6.8–18.5 (mean = 12.1, SD = 2.8), 2.6–4.8 (mean = 3.7, SD = 0.4), and 2.7–5.2 (mean = 3.4, SD = 0.5), respectively (Figure 4). The compositional differences within JFR lavas are best observed by considering the following two groups: (1) lavas of the Robinson Crusoe Island and nearby Alpha Seamount; and (2) lavas from Alejandro Selkirk Island together with samples from O'Higgins Guyot. For example, the ratios of some HFSEs differ for different volcanoes, Alpha and Robinson Crusoe samples have elevated Nb (for a given Zr) contents compared to O'Higgins and Alejandro Selkirk samples (Table 3 and Figure 4). The mean Nb/Zr ratios for O'Higgins, Alpha, Robinson Crusoe, and Alejandro Selkirk samples are 0.12, 0.16, 0.16, and 0.11, respectively (Figure 4; SD for all volcanoes is ± 0.01). The ratios of strongly incompatible elements such as Ta/Th and less incompatible elements such as Ti/Eu also differ by volcano, with the lowest values also found in Alejandro Selkirk/O'Higgins lavas.

4.4 Radiogenic isotopes

The young age (< 9.5 Ma) of JFR shield-building volcanism allows a direct evaluation of measured isotope data since the correction for radiogenic ingrowth over this period is negligible. All analyzed isotopic ratios show narrow ranges: ⁸⁷Sr/⁸⁶Sr = 0.70350–0.70376;

$^{143}\text{Nd}/^{144}\text{Nd} = 0.51281\text{--}0.51290$; $^{206}\text{Pb}/^{204}\text{Pb} = 19.05\text{--}19.29$; $^{207}\text{Pb}/^{204}\text{Pb} = 15.60\text{--}15.61$; and $^{208}\text{Pb}/^{204}\text{Pb} = 38.94\text{--}39.14$ (Table 4). Our Sr and Nd isotope data agree well with the literature and almost completely overlap the published Sr and Nd isotope data. The Sr vs. Nd isotope correlation diagram indicates a crude negative correlation, which might reflect the mixing of depleted (DM and/or HIMU) and enriched (EM) mantle components.

The ranges of Pb isotope ratios, particularly $^{207}\text{Pb}/^{204}\text{Pb}$, in our data ($^{206}\text{Pb}/^{204}\text{Pb} = 18.9\text{--}19.3$; $^{207}\text{Pb}/^{204}\text{Pb} = 15.59\text{--}15.68$; and $^{208}\text{Pb}/^{204}\text{Pb} = 38.9\text{--}39.3$) were narrow compared to published data (Gerlach et al., 1986; Baker et al., 1987; Truong et al., 2018). The considerably larger ranges in the literature data likely reflect within-run fractionation and/or problems with Pb-DS application and deconvolution, as indicated by unusual NBS981 values (i.e., high $^{207}\text{Pb}/^{204}\text{Pb}$ and $^{208}\text{Pb}/^{204}\text{Pb}$ values above the uranium and thorogenic correlation of published DS and TS NBS981 data). On all Sr–Nd–Pb isotope correlation diagrams, the data show intermediate compositions, similar to those of common components PREMA, C, and FOZO. These data might be interpreted as a mixture of various OIB end-members (Figure 5) (e.g., Zindler and Hart, 1986; Hanan and Graham, 1996; Stracke et al., 2005; White, 2015; Kimura et al., 2016). The data correlate well ($r^2 = 0.85$) on the thorogenic Pb isotope diagram, which might reflect the mixing of HIMU and EM1 components. Furthermore, high values of $^{208}\text{Pb}/^{204}\text{Pb}$ (for a given $^{206}\text{Pb}/^{204}\text{Pb}$; $\Delta 8/4 = 22.8 \pm 3.9$ in the data set presented here; cf., Hart, 1984) relative to DM and MORB, as seen in the East Pacific Rise (Macdougall and Lugmair, 1985) and the North Chile Ridge (Bach et al., 1996) lavas (Figure 5), indicate the presence of a DUPAL signature, a classical feature of the southern hemisphere.

Alejandro Selkirk/O'Higgins samples are characterized by low $^{206}\text{Pb}/^{204}\text{Pb}$ and $^{208}\text{Pb}/^{204}\text{Pb}$ along with high $^{143}\text{Nd}/^{144}\text{Nd}$, while the $^{207}\text{Pb}/^{204}\text{Pb}$ and $^{87}\text{Sr}/^{86}\text{Sr}$ values of these samples largely overlap with those of the Robinson Crusoe/Alpha lavas (Table 4). On the

uranogenic and thorogenic Pb isotope diagrams, it is clear that an end-member with more radiogenic $^{207}\text{Pb}/^{204}\text{Pb}$ and $^{208}\text{Pb}/^{204}\text{Pb}$ compared to DM is required; thus, EM1 is the only possible candidate (Figure 5). On the other hand, the Robinson Crusoe group projects to an end-member with radiogenic Pb (HIMU).

5. Discussion

5.1 Low-temperature alteration

The petrographically observed secondary minerals (opaques, clays, and iddingsite replacing phenocrysts and groundmass or filling vesicles) provide evidence for low-temperature alteration in some shield-stage lavas from JFR. The observed alteration and low-temperature mobility can explain the lower or higher values of some LILEs (e.g., Rb and Ba) compared to the values expected from melting and differentiation (Figure S.3). These features are typical of submarine lava samples worldwide (e.g., Hart and Nalwalk, 1970). However, Figure S.1 shows reasonably good correlations between Nb and Na, K, and U, suggesting that these elements were not completely mobilized. Even though alteration may have affected the mobility of these elements, they can still be used with caution for petrogenetic interpretations, at least in classification diagrams such as TAS (Figure 3).

5.2 Differentiation and primary melts

Fractional crystallization and the incorporation of primitive olivine antecrysts can explain the internal geochemical variations in rocks with the highest Mg# values ('olivine-rich' group) from Robinson Crusoe Island (Reyes et al., 2017). This interpretation can be extended to all JFR shield-building stage lavas, for which elevated Ni contents are observed in samples with high Mg# (Figure 2), and olivine crystals are out of equilibrium with their liquids (Reyes et al., 2017). Rocks in the 'near-primitive' group have experienced

little or no olivine fractionation/accumulation along with no significant clinopyroxene or plagioclase fractionation, as indicated by the constant $\text{CaO}/\text{Al}_2\text{O}_3$ ratios, for example (Figure 2). Some samples from this group could represent differentiated liquids mixed with primitive melts from magmatic recharge, which was also observed by Natland (2003), resulting in an increase in their MgO content.

Rocks from the 'differentiated' group were formed by fractional crystallization in shallow magmatic reservoirs (Reyes et al., 2017), with clinopyroxene fractionation playing an important role in addition to olivine fractionation, as indicated by the decreases in $\text{CaO}/\text{Al}_2\text{O}_3$ and Sc with decreasing Mg# (Figure 2). While the fractionation of other minerals such as plagioclase is less clear, it occurs at least in the Alejandro Selkirk lavas (see Mg# vs. Sr in Figure 2 and Mg# vs. Al_2O_3 in Figure S.2), because negative Eu anomalies are observed in a few samples (see Figure S.3). Although some variation is observed at a given Mg#, the magnitudes of Ti, Nb, and Ta enrichment are generally high, suggesting an origin of the 'TITAN' anomaly of JFR in the mantle source. Fractional crystallization can only partially modify the contents of these elements; it cannot explain the observed elevated Ti/Ti^* , Nb/Nb^* , and Ta/Ta^* ratios independent of Mg# (Figure 4). To accurately determine the phases involved in magma evolution, we modelled the fractional crystallization in our samples using COMAGMAT 3.72 software (Ariskin, 1999; Ariskin and Barmina, 2004).

The results of the model (see Appendix A for model input details) indicate the initial fractionation of olivine followed by clinopyroxene (high-pressure fractionation) and then plagioclase in Robinson Crusoe melts. In Alejandro Selkirk lavas, the olivine fractionation is followed by low pressure fractionation of plagioclase. This difference in crystallization sequence is consistent with the kink in the $\text{CaO}/\text{Al}_2\text{O}_3$ ratio at ~54 Mg# observed in Alejandro Selkirk lavas (Figure 6). The model also confirms the suitability of the chosen

samples as the parental magma, which is defined as the most magnesian liquid that can be inferred from a given rock suite (Herzberg et al., 2007). Samples LL040213-2 and MF-3 are particularly suitable since they generally satisfy the geochemistry of major and incompatible elements (rare earth elements and La/Yb) of JFR basic lavas (Figure 6).

All mafic samples of the JFR are ultimately derived from primary magmas, which are defined as melts originating as a partial melt of a mantle source (Herzberg et al., 2007). A critical goal is to infer the primary melt compositions to reveal the temperatures, pressures, and degrees of melting. For this purpose, we used the PRIMACALC2 model (Kimura and Ariskin, 2014), which employs the thermodynamic fractional crystallization model COMAGMAT 3.72, to examine the mantle equilibrium and trace element compositions of primary basalts with reverse and forward calculations in the parental magmas mentioned above. Both COMAGMAT 3.72 and PRIMACALC2 are applicable to tholeiitic to mildly alkalic OIBs and thus are also applicable to JFR shield lavas. The calculation conditions were the same as those used in the fractional crystallization model (see Appendix A), and the results are consistent between them (no significant differences in incompatible elements), especially for Alejandro Selkirk lavas (Table 5 and Figure 6). The H₂O content is a critical input in PRIMACALC2. However, due to the chemical similarity between the 'near-primitive' and primary melts in the JFR, no changes or only very subtle changes were observed in major and trace elements when the water content was changed.

5.3 Sources of magmatism in the JFR: peridotite and pyroxenites

Radiogenic isotopes (Sr, Nd, and Pb) show that the JFR shield-building lavas have enriched signatures with FOZO-type compositions (Figure 5). FOZO is a common composition observed in many OIB systems and is commonly interpreted as a mixture of other components (DM, HIMU, EM1, and EM2) (e.g., Hart et al., 1992; White, 2015; Kimura et al., 2016). The FOZO signature reflects the chemical heterogeneity in recycled

oceanic crust; which produces heterogeneous isotope ratios (e.g., Stracke et al., 2005); or relatively young recycled oceanic crust (Hanan and Graham, 1996). Furthermore, HIMU has been classically interpreted as igneous crust recycled back into the mantle in subduction zones that evolved isotopically over time (e.g., Zindler and Hart, 1986; Weaver, 1991; Hauri and Hart, 1993; Salters and White, 1998; Stracke et al., 2003; Stracke et al., 2005; Kimura et al., 2016). In the JFR, the Sr vs. Nd isotope diagram (Figure 5) along with the $^{206}\text{Pb}/^{204}\text{Pb}$ vs. Sr and Nd data can be explained by the mixing of HIMU and EM1 components, although separate mixing curves would be required to explain the Robinson Crusoe/Alpha and Alejandro Selkirk/O'Higgins trends. These separate mixing curves could be generated if isotopically identical end-members had different Sr/Nd, Sr/Pb, and Nd/Pb ratios, possibly reflecting different degrees of melting of the end-members. Alternatively, the two groups might simply reflect two different flavors of a common PREMA, C, or FOZO component. Thus, to explain the JFR isotopic signature, recycled material (likely oceanic crust and/or other mafic lithologies plus sediments) must have played an important role.

The JFR shield lavas satisfy some first-order geochemical features that have been interpreted as evidence of mafic lithologies different from peridotite in the source of OIB (considering only samples in the 'near-primitive' group to avoid clinopyroxene or plagioclase being on the liquid line of descent). The high TiO_2 content compared to MORB (Figure 7), for example, requires the involvement of a mafic lithology such as recycled oceanic crust (Prytulak and Elliot, 2007). In addition, the values of FC3MS ($\text{FeO}/\text{CaO} \times 3\text{MgO}/\text{SiO}_2 = 0.53$ for Robinson Crusoe and 0.60 for Alejandro Selkirk) are close to the maximum acceptable value for peridotite sources (0.65) and near the average value of pyroxenitic sources (0.46) (Yang and Zhou, 2013). The high values of Fe/Mn at a given MnO (Liu et al., 2008; Hoang et al., 2018) and low value of CaO for a given MgO (below the boundary for peridotites) imply pyroxenitic sources (Figure 7) (Herzberg, 2006;

Herzberg and Asimow, 2008). To refine these observations and explain the JFR trace-element geochemistry, we ran a basic qualitative model of the partial melting of lherzolite/garnet peridotite and recycled basalt without the involvement of sediments using the parameters of Stracke et al. (2003). We note that the 'TITAN' (Jackson et al., 2008) anomaly and heavy rare earth element (HREE) values (Figure 4) cannot be explained exclusively by derivation from a garnet or spinel peridotite source, and the involvement of recycled basalt is necessary.

When oceanic crust is recycled by subduction, it is dehydrated and metamorphosed and becomes capable of reacting with the surrounding mantle to generate olivine-free rocks such as pyroxenites, which could be part of the sources of a variety of magmas (Yaxley and Green, 1998; Kogiso et al., 1998; Hauri, 2002; Kogiso et al., 2003; Sobolev et al., 2005; Sobolev et al., 2007; Mallik and Dasgupta, 2012; Rosenthal et al., 2014). Thus, the isotopic and chemical evidence support the presence of mafic recycled material, particularly pyroxenites, as a minor but relevant component in the source of JFR magmas.

Considering that the volume of pyroxenites can make up to 10% of the mantle source (Pearson and Nixon, 1996; Stracke et al., 2003), in addition to the above-mentioned evidence, the involvement of pyroxenites in the JFR source is plausible. The importance of pyroxenite in the source has been reported for many intraplate oceanic islands such as the Canary Islands (e.g., Gurenko et al., 2006, 2009, 2010; Day et al., 2009; Klügel et al., 2017), Hawaii (e.g., Herzberg, 2006; García et al., 2015), Madeira (Gurenko et al., 2013), Mauritius (Paul et al., 2005), and the Galápagos (Trela et al., 2015).

5.4 Mantle source modeling

Considering the proposed presence of pyroxenite in the source, we attempted to quantify its abundance in the mantle plume beneath the JFR and determine the thermodynamic

parameters for the peridotite/pyroxenite source. Some models have been proposed to constrain the melting of mantle pyroxenites, including OBS1 (Kimura and Kawabata, 2015) and Melt-Px (Lambart et al., 2016). These models are primarily based on the parameterization of: (1) adiabatic decompression melting of peridotitic mantle containing pyroxenite veins by Phipps Morgan (2001); and (2) hydrous mantle melting by Katz et al. (2003). We used the OBS1 model because it considers the mixing of melts from peridotite and pyroxenite along with the metasomatic effect through which pyroxenitic melts generate in the surrounding 'ambient' peridotite (a mixture of enriched and depleted compositions). Considering the differences in melting temperatures between peridotite and pyroxenite (e.g., Pertermann and Hirschmann, 2003; Kogiso et al., 2003; Lambart et al., 2016), the metasomatic model seems more realistic than simple mixing of peridotite/pyroxenite melts. The OBS1 model explores five source parameters: pyroxenite fraction, Px_{fr} ; enriched peridotite fraction, $Per2_{fr}$; depleted peridotite fraction, $100 - [Px_{fr} + Per2_{fr}]$; potential temperature, T_p ; and pressure at melting termination, P_{mt} . The model compares the melts generated under these conditions with the 'near-primitive' melts of the JFR and saves the compositions that satisfy the fitting window shown in Table 6. PxF_{mt} , $PerF_{mt}$, and $TotF_{mt}$ represent the degree of melting at melting termination (in wt%) for pyroxenite, metasomatized peridotite, and the total mixture, respectively. Table 6 and Appendix B provide details of the input parameters used in the model; briefly, pyroxenite has a N-MORB composition (Pearce and Parkinson, 1993), enriched peridotite has a primitive mantle composition (Sun and McDonough, 1989), depleted peridotite has a depleted mantle composition (Workman and Hart, 2005), and the source contains 0.03 wt% H₂O. These parameters are the same as those used by Kimura and Kawabata (2015) and were chosen to simplify the comparisons between the results (especially for T_p).

The water content of the source is a critical parameter of the model; however, its value in the JFR source is unknown. To elucidate the effect of water in the model, we compared the results of the four main parameters (T_p , Px_{fr} , P_{mt} , $TotF_{mt}$) for each primary magma at different water contents (0, 0.03, and 0.06 wt%). Figure 8 shows that increasing the water content of the source resulted in a marked decrease in T_p , a subtle change in P_{mt} , and no changes in the other parameters. For instance, the average values of T_p for Alejandro Selkirk melts were 1404°C, 1371°C, and 1354°C for water contents of 0, 0.03, and 0.06 wt% H₂O, respectively; the corresponding values of P_{mt} in the same samples were 2.65, 2.56, and 2.51 GPa, respectively. In general, the values of Px_{fr} and $TotF_{mt}$ remained relatively constant with changing water content (Figure 8).

The main results of the model (details of model parameters can be found in Appendix B, and complete results in Table S.3) are shown in Table 7. The results confirm the presence of pyroxenite in the heterogeneous mantle plume beneath the JFR. The values of Px_{fr} ranged from 0.4–18.4 wt%, and T_p was relatively low (1312°C–1412°C). The values of $TotF_{mt}$ were highly variable (2.4–19.2 wt%), whereas P_{mt} showed a limited range (2.30–2.74 GPa).

Considering only the most representative primary melts (obtained from sample LL040213-2 for Robinson Crusoe Island and sample MF-3 for Alejandro Selkirk Island), the results of the model indicate relatively low- T_p (1316°C–1366°C for Robinson Crusoe melts and 1334°C–1412°C for Alejandro Selkirk melts at the source water content of 0.03 wt%) compared to the Kea trend magmas of Hawaii (1521°C–1596 °C;) (Herzberg and Gazel, 2009) and general OIB estimates (average of ~1596°C ± 38°C) (Putirka, 2008). Other OIBs yield lower T_p estimates, such 1342°C–1461°C for the Azores, 1419°C–1476°C for the Canary Islands, and 1452°C–1469°C for Iceland (Herzberg and Gazel, 2009). Gambier in the Pitcairn chain yielded a T_p of ~1400°C (Delavault et al., 2015). These T_p values

overlap with the upper range and extend to slightly higher values than the 'ambient' mantle with $T_p = 1280^{\circ}\text{C}$ – 1400°C (Herzberg et al., 2007), $\sim 1350^{\circ}\text{C}$ (Herzberg and Gazel, 2009), and $\sim 1396^{\circ}\text{C}$ (Putirka, 2008). Using the OBS1 model, Kimura and Kawabata (2015) estimated T_p values in the range of 1402°C – 1436°C (dry conditions) and 1381°C – 1389°C (source water content = 0.03 wt%, similar to the model used to determine our estimates) for the Loa trend magmas in Hawaii and 1300°C – 1310°C for MORB melts. This confirms that the JFR lavas have intermediate T_p values (1316°C – 1412°C) between some OIBs and ambient mantle.

We applied two additional geothermometers based on the MgO contents of primary magmas (Table 5). In both cases, the obtained T_p was higher than that estimated by OBS1. Specifically, using the method of Herzberg and Gazel (2009), we obtained T_p values of 1468°C for Robinson Crusoe samples and 1502°C for Alejandro Selkirk samples (error of $\sim 50^{\circ}\text{C}$ – 70°C). However, Mallik and Dasgupta (2014) reported that the presence of pyroxenite in the source results in an approximately 88°C overestimation in T_p based on the method of Herzberg and Gazel (2009) because this geothermometer is only calibrated for peridotites. Using the method of Liu et al. (2017), we obtained T_p values of 1446°C for Robinson Crusoe lavas and 1483°C for Alejandro Selkirk lavas. If pyroxenite is in the source, the T_p could be overestimated by $\sim 70^{\circ}\text{C}$. Accounting for the presence of pyroxenite in the source, the results obtained using OBS1, and especially the higher values, are consistent with the method of Herzberg and Gazel (2009) and Lui et al. (2017).

The T_p of $\sim 1582^{\circ}\text{C}$ obtained by Putirka (2008) for the JFR is $\sim 250^{\circ}\text{C}$ higher than our result. However, that estimate may be affected by methodological problems because the GEOROC database (used in that study) includes shield (with numerous 'olivine-rich' samples) and rejuvenated samples from the JFR. Olivines in basanites from the rejuvenated-stage have high Fo content implying high estimates of their source T_p . Thus,

the use of average values for the JFR based on the GEOROC database is questionable due to the contrasting geochemistry of the shield and rejuvenated samples. For more details on these differences, refer to Reyes et al. (2017).

Our relatively low- T_p might be explained by the cooling of the upwelling plume caused by the low ascent velocity of pyroxenite-bearing mantle plumes as a result of their density (Herzberg, 2011) along with the content of water (0.03 wt%). The addition of 0.03 wt% water reduces the solidus temperature on average by 17°C–32°C (Figure 8) (e.g., Kushiro et al., 1968; Gaetani and Groove, 1998). Assuming dry conditions, the mean T_p values are 1392°C for Robinson Crusoe lavas and 1404°C for Alejandro Selkirk lavas.

The differences in major and trace elements indicate variations in the degree of melting between the islands. These variations may be primarily related to the melting temperature, which is reflected in the T_p estimates but is technically not resolvable. The 30°C difference in mean T_p between the islands (for a water content of 0.03 wt% in the source) (Figure 9) is also found in the T_p estimates obtained by the alternative methods considered (differences of 34°C for the method of Herzberg and Gazel (2009) and 37°C for the method of Liu et al. (2017)). Although Devey et al. (2000) proposed the existence of a carbonated plume beneath the JFR, the presence of CO₂ was not considered in this study because the models used and T_p for other OIBs are not valid in carbonated systems. If we considered CO₂ in the source, the value of T_p should be lower, and the comparisons would be invalid.

The P_{mt} values (2.42–2.68 GPa in Robinson Crusoe magmas and 2.38–2.74 GPa in Alejandro Selkirk magmas) are probably related to the lithosphere–asthenosphere boundary. Based on an age-dependent half-space cooling model (Tassara et al., 2006), this boundary is thought to lie 60–75 km beneath the present position of the Robinson Crusoe and Alejandro Selkirk Islands along with the volcanoes located to the west (e.g.,

Friday and Domingo; Devey et al., 2000) and 75–90 km under the eastern segment of the JFR (including O'Higgins Guyot).

Some elements do not exactly satisfy the geochemical features of primary basalts (e.g., Pr, Sr, and Hf). These variations can be explained by subtle differences between the real sources involved and the compositions considered in the model, for example, enrichment in middle rare earth elements in the peridotite and/or pyroxenite beneath the JFR with respect to model sources: DM (Workman and Hart, 2005), PM (Sun and McDonough, 1989), and/or N-MORB (Pearce and Parkinson, 1993).

In addition to the differences in T_p discussed above, other noticeable differences are found between the results obtained for the different primary magmas of the JFR. Compared to the Alejandro Selkirk lavas, the Robinson Crusoe lavas yielded lower values of Px_{fr} (0.6–8.8 vs. 6.0–18.4 wt%), $PerF_{mt}$ (1.3–4.0 vs. 2.5–7.5 wt%), and PxF_{mt} (33.8–53.9 vs. 42.4–66.2 wt%), which are reflected in the different $TotF_{mt}$ values (3.4–7.4 vs. 7.2–19.2 wt%; Figure 9).

Despite the low mass content of pyroxenite in the source, the JFR lavas have marked pyroxenite signatures, which are interpreted to represent recycled oceanic crust. This can be explained by a stronger contribution of the pyroxenitic component to the primary melt compared to peridotite. Due to its thermodynamic characteristics, pyroxenite has a lower solidus temperature than peridotite; thus, its melting begins at a greater depth, and its melts can be extracted over a longer melting interval. This implies a greater pyroxenite contribution to the melt relative to its weight fraction in the source (greater by a factor of 5 to >10) (e.g., Pertermann and Hirschmann, 2003; Kogiso et al., 2003; Sobolev et al., 2007; Lambart et al., 2016). According to the model, the values of Px_{fr} are 0.6–8.8 wt% in the Robinson Crusoe lavas and 6.0–18.4 wt% in the Alejandro Selkirk lavas, whereas the proportions of pyroxenite component in the melt are 8.1%–69.3% and 40.7%–69.7%,

respectively (calculated as $Px_{fr} \times Px_{F_{mt}} / (Per_{F_{mt}} + Px_{fr} \times Px_{F_{mt}}) \times 100$). The enrichments in LILEs and light rare earth element (visible in Figure 9; see also Figure S.3), high values of Nb/Zr, and the more marked pyroxenitic signature in Robinson Crusoe lavas can be explained by the higher proportion of the more incompatible elements entering the melt at a low degree of melting, with the increase in less incompatible elements (e.g., HREEs) being more modest (Figure 4). Furthermore, source composition (e.g., an enrichment of some elements) could also influence the abundance of incompatible elements in the melts.

To check the above results, we also modeled two primary compositions obtained from parental samples (sample LL250711-7 from Robinson Crusoe Island and sample MF-6 from Alejandro Selkirk Island; black stars in Figure 6) with relatively low La/Yb ratios respect to the most representative samples. The results of the model show a minor decrease in the values of T_p , P_{mt} , Px_{fr} , and $TotF_{mt}$ compared to those obtained earlier (Figure S.4). Thus, despite the uncertainty, the results seem to be valid, at least from a qualitative point of view.

5.5 Petrogenesis and magmatic evolution

Based on the Farley et al. (1993) scheme, Truong et al. (2018) proposed a common but slightly heterogeneous mantle source for the JFR suite based on Sr–Nd–Pb systematics with variable $^3\text{He}/^4\text{He}$. With better geochronological constraints and more precise Pb isotope data, we are able to explain the variety of first-order features of the shield-stage lavas resulting from melting at different conditions over time and subtle compositional variations in the source. Truong et al. (2018) proposed that the JFR shield-stage can be divided into early (samples from Robinson Crusoe Island) and late (samples from Alejandro Selkirk Island) stages. However, that scheme does not reflect the magmatic evolution because, for example, the samples (LL260112-4 and LL250112-1) from Alejandro Selkirk with isotopic values closest to Robinson Crusoe (Group III) are found at

the base of the stratigraphic pile of the island, not at the summit (e.g., sample JR180913-1), as would be expected from the model of Truong et al (2018).

We propose that the JFR shield-stage involved the melting of a relatively low-temperature upwelling mantle plume with heterogeneous composition (with slight differences in isotope ratios and incompatible element abundances) and lithology (consisting of pyroxenite and peridotite). This plume mantle melted by decompression as it ascended to the lithosphere–asthenosphere boundary, with pyroxenite beginning to melt before peridotite. The differences between Robinson Crusoe/Alpha and Alejandro Selkirk/O’Higgins samples would be better explained in terms of natural variations of the FOZO source and temporal changes in the degree of melting generated by an increase of $\sim 30^{\circ}\text{C}$ in T_p in the Alejandro Selkirk/O’Higgins source material.

The low- T_p could also explain the weak geophysical signal of the JFR plume (Montelli et al., 2006), which reconciles the existence of intraplate volcanism with an absence of clear geophysical evidence for an ascending mantle plume. French and Romanowicz (2015) refer to the JFR plume as “somewhat resolved,” with a buoyancy flux value of $1.6 \text{ Mg}\cdot\text{s}^{-1}$ (Davies, 1988; Sleep, 1990). This value is similar to those of Iceland, Samoa, Cape Verde, Tristan, and Reunion, but higher than those of Canaries, Louisville, Galápagos, Kerguelen, and Azores, for which the plumes have higher potential temperatures (e.g., Herzberg and Gazel, 2009). Thus, the JFR would have been formed by a weak plume with a low- T_p that primarily produces melts from pyroxenite. In the absence of a large pyroxenitic component, sufficient melt would not be produced and hence a no hotspot track formed. Thus, melting in the JFR would be more related to the chemical properties than the thermal properties of the plume.

6. Conclusions

The O'Higgins Guyot, Alpha Seamount, Robinson Crusoe Island, and Alejandro Selkirk Island are large volcanic edifices of the JFR on the Nazca Plate. These features are primarily controlled by tholeiitic, transitional, and alkali basaltic shield-building stage volcanism. Their differentiation is controlled by fractional crystallization (including accumulation) and mixing/magmatic recharge. The age progression of the shield volcanism and the high $^3\text{He}/^4\text{He}$ (up to $18R_A$) indicate that the JFR was formed by a mantle plume. Whole-rock geochemical and Sr–Nd–Pb isotopic data (e.g., low CaO at a given MgO, a moderate 'TITAN' anomaly, and a PREMA/C/FOZO-type isotopic composition) suggest the existence of lithological heterogeneities in the plume source, pointing to the presence of both pyroxenite (derived from young, recycled oceanic crust) and peridotite in the source. A petrogenetic model based on incompatible element patterns for the most representative primary melts based on the Robinson Crusoe and Alejandro Selkirk 'near-primitive' samples indicate a relatively low- T_p compared to classical OIBs, a notable contribution of pyroxenite, and a depth of melting termination coherent with the lithosphere–asthenosphere boundary. The more marked chemical enrichment of Robinson Crusoe samples relative to Alejandro Selkirk lavas is related to natural heterogeneities of FOZO source and a lower degree of melting, which might reflect the difference in T_p of ~30 °C. In summary, we propose that a weak, low- T_p , pyroxenite-bearing, mantle plume is involved in the petrogenesis of the shield volcanism along the JFR.

Acknowledgments

This research was supported by the FONDECYT 1110966 and 1141303 (both granted to L.E. Lara) and FONDAP 15090013 projects along with research funds from the GEOMAR Helmholtz Centre for Ocean Research Kiel. The main results presented in this manuscript are part of the first author's doctoral thesis, which is supported by a CONICYT fellowship. The authors are grateful to C. Herzberg, two anonymous reviewers, and the associate

editor A. Stracke for providing constructive reviews that improved this paper. We also acknowledge the Scripps Institution of Oceanography for samples from Alpha Seamount and Alejandro Selkirk Island, the SO101 CONDOR cruise for samples from O'Higgins Guyot and the CIMAR 22 for samples from the Alpha Seamount. Finally, we thank J-L. Paquette, D. Auclair, and C. Bosq from Clermont-Ferrand for performing some of the Sr–Nd analyses. CONAF authorized scientific research in this protected area, and DIFROL provided logistical support during the 2013 field campaign.

Appendix A. Fractional crystallization model

The starting compositions for the COMAGMAT 3.72 (Ariskin and Barmina, 2004) fractional crystallization model were three samples from Robinson Crusoe Island and three from Alejandro Selkirk Islands to account for the internal variations in La/Yb ratios observed in each volcano. The starting compositions were selected as parental candidates from the 'near-primitive' or 'olivine-rich' groups based on their chemical characteristics (e.g., high Mg# and moderate enrichment in Ni and Cr). The most representative samples (with intermediate values of La/Yb) were sample LL040213-2 for Robinson Crusoe Island (similar to Alpha Seamount) and sample MF-3 for Alejandro Selkirk Island (similar to O'Higgins Guyot). Other selected samples (LL250711-7 for Robinson Crusoe Island and MF-6 for Alejandro Selkirk Island) represent groups constituted by few samples with La/Yb values lower than the dominant values. The pressure of fractionation was fixed at 2.0 kbar (taken from Reyes et al., 2017), and redox conditions were set at the QFM (quartz-fayalite-magnetite) buffer, as recommended for OIBs by Kimura and Ariskin (2014). The crystallization increment was 0.1%. Magmatic water contents are problematic since no direct measurements of water content in JFR lavas are available. Putirka (2008) estimated a water content of 1.91 wt% based on the calculated degree of partial melting (F) and typical H₂O/Ce ratios for the ocean island sources (Dixon et al., 2002). However, this value

may include error caused by potential problems in the estimation of F and temperature because the data considered in the calculations were taken from the GEOROC database, which primarily includes data from Farley et al. (1993). While Farley et al. (1993) included samples from different stages of volcanism, sampling was skewed towards picrites containing accumulated olivine because their goal was to analyze $^3\text{He}/^4\text{He}$ retained in mafic phenocrysts. Using the same estimate as Dixon et al. (2002) (i.e., $\text{H}_2\text{O}/\text{Ce} = 200$ in Pacific FOZO) but only in the most primitive magmas, we obtained a water content of ~ 0.80 wt% for the JFR. This value was used as input in the model and seems to be reasonable considering other estimates (e.g., 0.9–1.0 wt% for the plume source end-member in the Easter/Salas y Gomez Seamount Chain, which is more enriched than the source of the JFR) (Simons et al., 2002).

Appendix B. OBS1 mantle source modeling

The OBS1 model compares the melts generated under five conditions explored by the Monte Carlo method [pyroxenite fraction (Px_{fr}); enriched peridotite fraction ($Per2_{fr}$); depleted peridotite fraction, $100 - (Px_{fr} + Per2_{fr})$; potential temperature (T_p); and pressure at melting termination (P_{mt})] with the primary melts of the studied system. The input parameters (fixed by the user) of the OBS1 model (Kimura and Kawabata, 2015) are primary melt, melting model, pyroxenite composition, enriched peridotite composition, and water content of the source. We used the primary melts calculated by PRIMACALC2 (see section 5.2) for the OBS1 model, considering that samples LL040213-2 and MF-3 are the most representative samples of the Robinson Crusoe/Alpha and Alejandro Selkirk/O'Higgins volcanoes, respectively. With respect to the melting model, metasomatic parameterization appears to be most realistic (Kimura and Kawabata, 2015) and was selected in this study. The differences in melting temperatures between peridotite and pyroxenite (e.g., Pertermann and Hirschmann, 2003; Kogiso et al., 2003; Lambart et al.,

2016) also support this choice. The different source compositions were taken from the literature; specifically, the average depleted mantle of Workman and Hart (2005) was used for the depleted peridotite, the primitive mantle of Sun and McDonough (1989) was used for enriched peridotite, and the N-MORB of Pearce and Parkinson (1993) was used for pyroxenite. According to the discussion in section 5.3, pyroxenites come from recycled oceanic crust (classically N-MORB). The effect of alteration in the ocean is limited to the top of the oceanic crust (Staudigel et al., 1996). Furthermore, subduction modification is difficult to estimate, but is thought to be less than 5% for REEs and HFSEs (Porter and White, 2009; Kimura and Ariskin, 2014). Thus, the simplification of considering N-MORB as the pyroxenite source is reasonable, particularly because the analysis is based mostly on the concentrations of generally immobile elements (i.e., Nb, Zr, La, and Yb).

For the sake of simplicity, we assumed a water content in the source of 0.03 wt% because no studies have been done on the water contents of magmas from the JFR. This value is the same used by Kimura and Kawabata (2015) in their estimates of T_p for the Hawaiian Lea trend using OBS1. The water content used in our model is lower than estimates for more enriched sources: 0.075 wt% for Pacific FOZO mantle (Dixon et al., 2002) and 0.075 wt% for the enriched plume end-member of the Easter hotspot track (Simons et al., 2002). However, our water content is slightly lower than the average value (0.053 wt%) reported by Kovalenko et al. (2006) for Type III magmas, which share some similarities with JFR shield lavas. Our water content is similar to the primitive mantle value of 0.033 wt% (Dixon and Clague, 2001). The assumed water content and the exclusion of CO₂ in the source represent important uncertainties in this study that are discussed in Section 5.4.

Finally, the fitting window was fixed at 200% for Th; 60% for Ta, Ce, Pr, and Sr; and 30% for Nd, Sm, Hf, Eu, Gd, Tb, Dy, Y, Ho, Er, Tm, and Lu. Although Rb, Ba, U, and K could be considered in OBS1, we not included them in our source modelling. This was done to

avoid uncertainties related to low-temperature alteration in a few JFR samples. Our model focuses on the behavior of Nb/Zr and La/Yb ratios, which are distinctive features among the JFR volcanoes. Hence, for these ratios along with Nb, Zr, La, and Yb, the fitting window was only 15%. A summary of the input parameters is provided in Table 6. After exploratory modeling, we ran 100,000 iterations or more until obtaining at least 50 successful results. Detailed results of the model are provided in Table S.3.

Appendix C. Supplementary data

Supplementary data associated with this article (Figures S.1, S.2, S.3 & S.3 and Tables S.1, S.2 and S.3) can be found in the online version, at XX.

References

- Anderson, D.L., 2000. The thermal state of the upper mantle; no role for mantle plumes. *Geophys. Res. Lett.* 27, 3623–3626. doi:10.1029/2000GL011533
- Anderson, D.L., 2001. Top-down tectonics? *Science* 293, 2016–2018. doi:10.1126/science.1065448
- Argus, D.F., Gordon, R.G., Heflin, M.B., Ma, C., Eanes, R.J., Willis, P., Peltier, W.R., Owen, S.E., 2010. The angular velocities of the plates and the velocity of Earth's centre from space geodesy. *Geophys. J. Int.* 180, 913–960. doi.org/10.1111/j.1365-246X.2009.04463.x
- Ariskin, A.A., 1999. Phase equilibria modeling in igneous petrology: use of COMAGMAT model for simulating fractionation of ferro-basaltic magmas and the genesis of high-alumina basalt. *J. Volcanol. Geotherm. Res.* 90, 115–162. doi.org/10.1016/S0377-0273(99)00022-0
- Ariskin, A.A., Barmina, G.S., 2004. COMAGMAT: Development of a magma crystallization model and its petrological applications. *Geochemistry Int.* 42, s1–s157. doi.org/scopus/2-s2.0-5444237530
- Astudillo, V., 2014. Geomorfología y evolución geológica de la isla Robinson Crusoe, Archipiélago Juan Fernández. Universidad de Chile (154 pp.).
- Bach, W., Erzinger, J., Dosso, L., Bollinger, C., Bougault, H., Etoubleau, J., Sauerwein, J., 1996. Unusually large NbTa depletions in North Chile ridge basalts at 36°50' to 38°56'S:

major element, trace element, and isotopic data. *Earth Planet. Sci. Lett.* 142, 223–240. doi.org/10.1016/0012-821X(96)00095-7

Baker, P.E., Gledhill, A., Harvey, P.K., Hawkesworth, C.J., 1987. Geochemical evolution of the Juan Fernandez Islands, SE Pacific. *J. Geol. Soc. London.* 144, 933–944. doi.org/10.1144/gsjgs.144.6.0933

Baker, J.; Peate, D.; Waight, T.; Mayzen, C., 2004. Pb isotopic analysis of standards and samples using a ^{207}Pb – ^{204}Pb double spike and thallium to correct for mass bias with a double-focusing MC-ICP-MS. *Chemical Geology* 211, 275–303. doi.org/10.1016/j.chemgeo.2004.06.030

Ballmer, M.D., van Hunen, J., Ito, G., Tackley, P.J., Bianco, T. a., 2007. Non-hotspot volcano chains originating from small-scale sublithospheric convection. *Geophys. Res. Lett.* 34. doi:10.1029/2007GL031636

Blichert-Toft, J., 1999. Hf isotope evidence for pelagic sediments in the source of hawaiian basalts. *Science* 285 (5429), 879–882. doi.org/10.1126/science.285.5429.879

Booker, J., Bullard, E.C., Grasty, R.L., 1967. Palaeomagnetism and age of rocks from Easter Island and Juan Fernandez. *Geophys. J. Int.* 12, 469–471. doi.org/10.1111/j.1365-246X.1967.tb03127.x

Boschi, L.; Becker, T.W.; Steinberger, B., 2007. Mantle plumes: Dynamic models and seismic images. *Geochemistry, Geophys. Geosystems* 8 (10). doi.org/10.1029/2007GC001733

Clouard, V., Bonneville, A., 2001. How many Pacific hotspots are fed by deep-mantle plumes? *Geology* 29(8), 695–698. doi:10.1130/0091-7613(2001)029<0695:HMPHAF>2.0.CO;2

Courtillot, V., Davaille, A., Besse, J., Stock, J., 2003. Three distinct types of hotspots in the Earth's mantle. *Earth Planet. Sci. Lett.* 205, 295–308. doi.org/10.1016/S0012-821X(02)01048-8

Davies, G. F., 1988. Ocean bathymetry and mantle convection: 1. Large-scale flow and hotspots, *J. Geophys. Res.*, 93(B9), 10467–10480. doi: 10.1029/JB093iB09p10467.

Day, J.M.D., Pearson, D.G., Macpherson, C.G., Lowry, D., Carracedo, J.-C., 2009. Pyroxenite-rich mantle formed by recycled oceanic lithosphere: Oxygen-osmium isotope evidence from Canary Island lavas. *Geology* 37, 555–558. doi.org/10.1130/G25613A.1

Delavault, H., Chauvel, C., Sobolev, A., & Batanova, V., 2015. Combined petrological, geochemical and isotopic modeling of a plume source: Example of Gambier Island, Pitcairn chain. *Earth and Planetary Science Letters*, 426, 23–35. doi.org/10.1016/j.epsl.2015.06.013

Devey, C.W., Hémond, C., Stoffers, P., 2000. Metasomatic reactions between carbonated plume melts and mantle harzburgite: the evidence from Friday and Domingo Seamounts (Juan Fernandez chain, SE Pacific). *Contrib. to Mineral. Petrol.* 139, 68–84. doi.org/10.1007/s004100050574

- Dixon, J.E., Leist, L., Langmuir, C., Schilling, J.-G., 2002. Recycled dehydrated lithosphere observed in plume-influenced mid-ocean-ridge basalt. *Nature* 420, 385–389. doi.org/10.1038/nature01215
- Dixon, J.E., Clague, D. a., 2001. Volatiles in basaltic glasses from Loihi Seamount, Hawaii: Evidence for a relatively dry plume component. *J. Petrol.* 42, 627–654. doi.org/10.1093/petrology/42.3.627
- Farley, K.A., Basu, A.R., Craig, H., 1993. He, Sr and Nd isotopic variations in lavas from the Juan Fernandez Archipelago, SE Pacific. *Contrib. to Mineral. Petrol.* 115, 75–87. doi.org/10.1007/BF00712980
- French, S.W., Romanowicz, B., 2015. Broad plumes rooted at the base of the Earth's mantle beneath major hotspots. *Nature* 525, 95–99. doi.org/10.1038/nature14876
- Gaetani, G.A., Grove, T.L., 1998. The influence of water on melting of mantle peridotite. *Contrib. to Mineral. Petrol.* 131, 323–346. doi.org/10.1007/s004100050396
- Garcia, M.O., 1996. Petrography and olivine and glass chemistry of lavas from the Hawaii Scientific Drilling Project. *Journal of Geophysical Research: Solid Earth* 101, 11701–11713. doi:10.1029/95JB03846
- Garcia, M.O., Smith, J.R., Tree, J.P., Weis, D., Harrison, L., Jicha, B.R., 2015. Petrology, geochemistry, and ages of lavas from Northwest Hawaiian Ridge volcanoes. *Geological Society of America Special Papers* 511. doi:10.1130/2015.2511(01)
- Geldmacher J, Hoernle K, van den Bogaard P, Hauff F, Klügel A (2008) Age and Geochemistry of the Central American Forearc Basement (DSDP Leg 67 and 84): Insights into Mesozoic Arc Volcanism and Seamount Accretion on the Fringe of the Caribbean LIP. *J. Petrology* 49: 1781-1815; doi:10.1093/petrology/egn046.
- Gerlach, D.C., Hart, S.R., Morales, V.W.J., Palacios, C., 1986. Mantle heterogeneity beneath the Nazca plate: San Felix and Juan Fernandez islands. *Nature* 322, 165–169. doi:10.1038/322165a0
- Gurenko AA, Hoernle KA, Hauff F, Schmincke H-U, Han D, Miura YN, Kaneoka I (2006) Major, trace element and Nd-Sr-Pb-O-He-Ar isotope signatures of shield stage lavas from the central and western Canary Islands: Insights into mantle and crustal processes. *Chemical Geology*, v. 233, p. 75-112. doi.org/10.1016/j.chemgeo.2006.02.016
- Gurenko AA, Sobolev AV, Hoernle KA, Hauff F, Schmincke H-U (2009) Enriched, HIMU-type peridotite and depleted recycled pyroxenite in the Canary plume: A mixed-up mantle. *Earth and Planetary Science Letters* 277(3-4):514-524. doi.org/10.1016/j.epsl.2008.11.013
- Gurenko A, Hoernle K, Sobolev A, Hauff F, Schmincke H-U (2010) Source components of the Gran Canaria (Canary Islands) shield stage magmas: evidence from olivine composition and Sr–Nd–Pb isotopes. *Contributions to Mineralogy and Petrology* 159: 689-702. DOI 10.1007/s00410-009-0448-8.

- Gurenko, A.A., Geldmacher, J., Hoernle, K.A., Sobolev, A. V., 2013. A composite, isotopically-depleted peridotite and enriched pyroxenite source for Madeira magmas: Insights from olivine. *Lithos* 170–171, 224–238. doi.org/10.1016/j.lithos.2013.03.002
- Hanan, B.B., Graham, D.W., 1996. Lead and helium isotope evidence from oceanic basalts for a common deep source of mantle plumes. *Science* 272 (5264), 991–995. doi:10.1126/science.272.5264.991
- Hart, S. R., & Nalwalk, A. J., 1970. K, Rb, Cs and Sr relationships in submarine basalts from the Puerto Rico trench. *Geochimica et Cosmochimica Acta*, 34(2), 145–155. doi.org/10.1016/0016-7037(70)90002-5
- Hart, S.R., 1984. A large-scale isotope anomaly in the Southern Hemisphere mantle. *Nature* 309, 753–757. doi.org/10.1038/309753a0
- Hart, S.R., Hauri, E.H., Oschmann, L.A., Whitehead, J.A., 1992. Mantle Plumes and Entrainment: Isotopic Evidence. *Science* 256 (5056), 517–520. doi.org/10.1126/science.256.5056.517
- Hauri, E.H., 2002. Osmium isotopes and mantle convection. *Philos. Trans. R. Soc. A Math. Phys. Eng. Sci.* 360, 2371–2382. doi.org/10.1098/rsta.2002.1073
- Hauri, E.H., Hart, S.R., 1993. Re-Os isotope systematics of HIMU and EMII oceanic island basalts from the south Pacific Ocean. *Earth Planet. Sci. Lett.* 114, 353–371. doi.org/10.1016/0012-821X(93)90036-9
- Herzberg, C., 2006. Petrology and thermal structure of the Hawaiian plume from Mauna Kea volcano. *Nature* 444, 605–609. doi.org/10.1038/nature05254
- Herzberg, C., Asimow, P.D., Arndt, N., Niu, Y., Leshner, C.M., Fitton, J.G., Cheadle, M.J., Saunders, A.D., 2007. Temperatures in ambient mantle and plumes: Constraints from basalts, picrites, and komatiites. *Geochemistry, Geophys. Geosystems* 8, Q02006. doi.org/10.1029/2006GC001390
- Herzberg, C., Asimow, P.D., 2008. Petrology of some oceanic island basalts: PRIMELT2.XLS software for primary magma calculation. *Geochemistry, Geophys. Geosystems* 9, Q09001. doi.org/10.1029/2008GC002057
- Herzberg, C., & Gazel, E., 2009. Petrological evidence for secular cooling in mantle plumes. *Nature*, 458(7238), 619–622. doi.org/10.1038/nature07857
- Hieronimus, C.F., Bercovici, D., 2000. Non-hot spot formation of volcanic chains: Controls of tectonic stresses on magma transport. *Earth Planet. Sci. Lett.* 181, 539–554. doi:10.1016/S0012-821X(00)00227-2
- Hoang, T. H. A., Choi, S. H., Yu, Y., Pham, T. H., Nguyen, K. H., & Ryu, J. S., 2018. Geochemical constraints on the spatial distribution of recycled oceanic crust in the mantle source of late Cenozoic basalts, Vietnam. *Lithos*, 296–299, 382–395. doi.org/10.1016/j.lithos.2017.11.020

- Hoernle, K., Abt, D.L., Fischer, K.M., Nichols, H., Hauff, F., Abers, G.A., van den Bogaard, P., Heydolph, K., Alvarado, G., Protti, M. and Strauch, W. (2008) Arc-parallel flow in the mantle wedge beneath Costa Rica and Nicaragua. *Nature* 451, 1094-1097.
- Hoernle, K., Hauff, F., Werner, R., van den Bogaard, P., Gibbons, A.D., Conrad, S., Müller, R.D., 2011. Origin of Indian Ocean Seamount Province by shallow recycling of continental lithosphere. *Nat. Geosci.* 4, 883–887. doi.org/10.1038/ngeo1331
- Hofmann, A. W., & White, W. M., 1982. Mantle plumes from ancient oceanic crust. *Earth and Planetary Science Letters*, 57(2), 421–436. doi.org/10.1016/0012-821X(82)90161-3
- Hofmann, A.W., 1988. Chemical differentiation of the Earth: the relationship between mantle, continental crust, and oceanic crust. *Earth Planet. Sci. Lett.* 90, 297–314. doi.org/10.1016/0012-821X(88)90132-X
- Homrighausen S, Hoernle K, Geldmacher J, Wartho J, Hauff F, Portnyagin M, Werner R, van den Bogaard P, Garbe-Schönberg D (2018a) Unexpected HIMU-type Late-Stage Volcanism on the Walvis Ridge. *Earth and Planetary Science Letters*, 492: 251-263. doi.org/10.1016/j.epsl.2018.03.049
- Homrighausen S, Hoernle K, Hauff F, Geldmacher J, Wartho J, van den Bogaard P, Garbe-Schönberg D (2018b) Global distribution of the HIMU end member: Formation through Archean plume-lid tectonics. *Earth-Science Reviews* 182: 85-101. doi.org/10.1016/j.earscirev.2018.04.009
- Jackson, M.G., Kurz, M.D., Hart, S.R., Workman, R.K., 2007. New Samoan lavas from Ofu Island reveal a hemispherically heterogeneous high $^3\text{He}/^4\text{He}$ mantle. *Earth Planet. Sci. Lett.* 264, 360–374. doi.org/10.1016/j.epsl.2007.09.023
- Jackson, M.G., Hart, S.R., Saal, A.E., Shimizu, N., Kurz, M.D., Blusztajn, J.S., Skovgaard, A.C., 2008. Globally elevated titanium, tantalum, and niobium (TITAN) in ocean island basalts with high $^3\text{He}/^4\text{He}$. *Geochemistry, Geophys. Geosystems* 9, Q04027. doi.org/10.1029/2007GC001876
- Jackson, M.G., Konter, J.G., Becker, T.W., 2017. Primordial helium entrained by the hottest mantle plumes. *Nature* 542, 340–343. doi.org/10.1038/nature21023
- Jochum, K. P., Weis, U., Schwager, B., Stoll, B., Wilson, S. A., Haug, G. H., Andreae, M. O. and Enzweiler, J., 2016. Reference Values Following ISO Guidelines for Frequently Requested Rock Reference Materials. *Geostand Geoanal Res*, 40: 333-350. doi:10.1111/j.1751-908X.2015.00392.x
- Katz, R.F., Spiegelman, M., Langmuir, C.H., 2003. A new parameterization of hydrous mantle melting. *Geochemistry, Geophys. Geosystems* 4, 1073. doi.org/10.1029/2002GC000433
- Kimura, J.-I., Gill, J.B., Skora, S., van Keken, P.E., Kawabata, H., 2016. Origin of geochemical mantle components: Role of subduction filter. *Geochemistry, Geophys. Geosystems* 17, 3289–3325. doi.org/10.1002/2016GC006343

- Kimura, J.-I., Ariskin, A.A., 2014. Calculation of water-bearing primary basalt and estimation of source mantle conditions beneath arcs: PRIMACALC2 model for WINDOWS. *Geochemistry, Geophys. Geosystems* 15, 1494–1514. doi.org/10.1002/2014GC005329
- Kimura, J.-I., Kawabata, H., 2015. Ocean Basalt Simulator version 1 (OBS1): Trace element mass balance in adiabatic melting of a pyroxenite-bearing peridotite. *Geochemistry, Geophys. Geosystems* 16, 267–300. doi.org/10.1002/2014GC005606
- Klügel, A., Galipp, K., Hoernle, K., Hauff, F., Groom, S., 2017. Geochemical and volcanological evolution of La Palma, Canary Islands. *J. Petrol.* 58, 1227–1248. doi.org/10.1093/petrology/egx052
- Kogiso, T., Hirose, K., Takahashi, E., 1998. Melting experiments on homogeneous mixtures of peridotite and basalt: application to the genesis of ocean island basalts. *Earth Planet. Sci. Lett.* 162, 45–61. doi.org/10.1016/S0012-821X(98)00156-3
- Kogiso, T., Hirschmann, M.M., Frost, D.J., 2003. High-pressure partial melting of garnet pyroxenite: possible mafic lithologies in the source of ocean island basalts. *Earth Planet. Sci. Lett.* 216, 603–617. doi.org/10.1016/S0012-821X(03)00538-7
- Kovalenko, V.I., Naumov, V.B., Giris, a. V., Dorofeeva, V. a., Yarmolyuk, V. V., 2006. Composition and chemical structure of oceanic mantle plumes. *Petrology* 14, 452–476. doi.org/10.1134/S0869591106050031
- Kushiro, I., Syono, Y., Akimoto, S., 1968. Melting of a peridotite nodule at high pressures and high water pressures. *J. Geophys. Res.* 73, 6023–6029. doi.org/10.1029/JB073i018p06023
- Lambart, S., Baker, M.B., Stolper, E.M., 2016. The role of pyroxenite in basalt genesis: Melt-PX, a melting parameterization for mantle pyroxenites between 0.9 and 5 GPa. *J. Geophys. Res. Solid Earth* 121, 5708–5735. doi.org/10.1002/2015JB012762
- Lara, L. E., Díaz-Naveas, J., Reyes, J., Jicha, B., Orozco, G., Tassara, A., & Kay, S., 2018a. Unraveling short-lived rejuvenated volcanism and a rapid transition from shield stage at O'Higgins Guyot, Juan Fernández Ridge, Pacific SE. *Deep-Sea Research Part I: Oceanographic Research Papers*, 141, 33–42. doi.org/10.1016/j.dsr.2018.08.012
- Lara, L. E., Reyes, J., Jicha, B. R., & Díaz-Naveas, J., 2018b. $^{40}\text{Ar}/^{39}\text{Ar}$ Geochronological Constraints on the Age Progression Along the Juan Fernández Ridge, SE Pacific. *Front. Earth Sci.* 6:194. doi.org/10.3389/feart.2018.00194
- Le Maitre, R.W., 2002. *Igneous rocks—a classification and glossary of terms*. Cambridge University Press, Cambridge (236 pp.). doi.org/10.1017/CBO9780511535581
- Liu, Y., Zong, K., Kelemen, P. B., & Gao, S., 2008. Geochemistry and magmatic history of eclogites and ultramafic rocks from the Chinese continental scientific drill hole: Subduction and ultrahigh-pressure metamorphism of lower crustal cumulates. *Chemical Geology*, 247(1–2), 133–153. doi.org/10.1016/j.chemgeo.2007.10.016

- Liu, J., Xia, Q. K., Kuritani, T., Hanski, E., & Yu, H. R., 2017. Mantle hydration and the role of water in the generation of large igneous provinces. *Nature Communications*, 8(1), 1824. doi.org/10.1038/s41467-017-01940-3
- Macdougall, J.D., Lugmair, G.W., 1985. Extreme isotopic homogeneity among basalts from the southern East Pacific Rise: mantle or mixing effect? *Nature* 313, 209–211. doi.org/10.1038/313209a0
- Mallik, A., Dasgupta, R., 2012. Reaction between MORB-eclogite derived melts and fertile peridotite and generation of ocean island basalts. *Earth Planet. Sci. Lett.* 329–330, 97–108. doi.org/10.1016/j.epsl.2012.02.007
- Mallik, A., Dasgupta, R., 2014. Effect of variable CO₂ on eclogite-derived andesite and lherzolite reaction at 3 GPa-Implications for mantle source characteristics of alkalic ocean island basalts. *Geochemistry, Geophys. Geosystems* 15, 1533–1557. doi.org/10.1002/2014GC005251
- Montelli, R., Nolet, G., Dahlen, F.A., Masters, G., 2006. A catalogue of deep mantle plumes: New results from finite-frequency tomography. *Geochemistry, Geophys. Geosystems* 7, Q11007. doi.org/10.1029/2006GC001248
- Morgan, W.J., 1971. Convection plumes in the lower mantle. *Nature* 230, 42–43. doi.org/10.1038/230042a0
- Morgan, W.J., 1972. Deep mantle convection plumes and plate motions. *Am. Assoc. Pet. Geol. Bull.* 56, 203–213. doi.org/10.1306/819A3E50-16C5-11D7-8645000102C1865D
- Natland, J.H., 2003. Capture of helium and other volatiles during the growth of olivine phenocrysts in picritic basalts from the Juan Fernandez Islands. *J. Petrol.* 44, 421–456. doi.org/10.1093/petrology/44.3.421
- Nobre Silva, I., Weis D., Barling J., Scoates J.S. 2009. Basalt leaching systematics and consequences for Pb isotopic compositions by MC-ICP- MS. *Geochemistry Geophysics Geosystems*, 10, Q08012, doi: 10.1029/2009GC002537.
- Othman, D. Ben, Polvé, M., Allègre, C.J., 1984. Nd-Sr isotopic composition of granulites and constraint on the evolution of the lower continental crust. *Nature*, 307, 510. doi.org/10.1038/307510a0
- Paul, D., White, W.M., Blichert-Toft, J., 2005. Geochemistry of Mauritius and the origin of rejuvenescent volcanism on oceanic island volcanoes. *Geochemistry, Geophys. Geosystems* 6, Q06007. doi.org/10.1029/2004GC000883
- Pearce, J. A., & Parkinson, I. J., 1993. Trace element models for mantle melting: application to volcanic arc petrogenesis. *Geological Society, London, Special Publications*, 76(1), 373–403. doi.org/10.1144/GSL.SP.1993.076.01.19
- Pearson, D.G., Nixon, P.H., 1996. Diamonds in young orogenic belts: graphitised diamonds from Beni Bousera, N. Morocco, a comparison with kimberlite-derived diamond

- occurrences and implications for diamond genesis and exploration. *Africa Geosci. Rev.* 3, 295–316.
- Pertermann, M., Hirschmann, M.M., 2003. Partial melting experiments on a MORB-like pyroxenite between 2 and 3 GPa: Constraints on the presence of pyroxenite in basalt source regions from solidus location and melting rate. *J. Geophys. Res. Solid Earth* 108, 1–17. doi.org/10.1029/2000JB000118
- Peters, B.J., Day, J.M.D., 2014. Assessment of relative Ti, Ta, and Nb (TITAN) enrichments in ocean island basalts. *Geochemistry, Geophys. Geosystems* 15, 4424–4444. doi.org/10.1002/2014GC005506
- Phipps Morgan, J., 2001. Thermodynamics of pressure release melting of a veined plum pudding mantle. *Geochemistry, Geophys. Geosystems* 2, n/a-n/a. https://doi.org/10.1029/2000GC000049
- Pin, C., Zalduegui, J.S., 1997. Sequential separation of light rare-earth elements, thorium and uranium by miniaturized extraction chromatography: Application to isotopic analyses of silicate rocks. *Anal. Chim. Acta* 339, 79–89. doi.org/10.1016/S0003-2670(96)00499-0
- Porter, K.A., White, W.M., 2009. Deep mantle subduction flux. *Geochemistry, Geophys. Geosystems* 10, Q12016. doi.org/10.1029/2009GC002656
- Prytulak, J., Elliott, T., 2007. TiO₂ enrichment in ocean island basalts. *Earth Planet. Sci. Lett.* 263, 388–403. doi.org/10.1016/j.epsl.2007.09.015
- Putirka, K., 2008. Excess temperatures at ocean islands: Implications for mantle layering and convection. *Geology* 36, 283–286. doi.org/10.1130/G24615A.1
- Reyes, J., Lara, L.E., Morata, D., 2017. Contrasting P-T paths of shield and rejuvenated volcanism at Robinson Crusoe Island, Juan Fernández Ridge, SE Pacific. *J. Volcanol. Geotherm. Res.* 341, 242–254. doi.org/10.1016/j.jvolgeores.2017.05.035
- Rodrigo, C., Lara, L.E., 2014. Plate tectonics and the origin of the Juan Fernandez Ridge: analysis of bathymetry and magnetic patterns. *Lat. Am. J. Aquat. Res.* 42, 907–917. doi.org/10.3856/vol42-issue4-fulltext-15
- Rosenthal, A., Yaxley, G.M., Green, D.H., Hermann, J., Kovács, I., Spandler, C., 2015. Continuous eclogite melting and variable refertilisation in upwelling heterogeneous mantle. *Sci. Rep.* 4, 6099. doi.org/10.1038/srep06099
- Salters, V.J., White, W.M., 1998. Hf isotope constraints on mantle evolution. *Chem. Geol.* 145, 447–460. doi.org/10.1016/S0009-2541(97)00154-X
- Simons, K., Dixon, J., Schilling, J.-G., Kingsley, R., Poreda, R., 2002. Volatiles in basaltic glasses from the Easter-Salas y Gomez Seamount Chain and Easter Microplate: Implications for geochemical cycling of volatile elements. *Geochemistry, Geophys. Geosystems* 3, 1–29. doi.org/10.1029/2001GC000173

- Sleep, N.H., 1990. Hotspots and mantle plumes: Some phenomenology. *J. Geophys. Res.* 95, 6715. doi.org/10.1029/JB095iB05p06715
- Sobolev, A. V., Hofmann, A.W., Sobolev, S. V., Nikogosian, I.K., 2005. An olivine-free mantle source of Hawaiian shield basalts. *Nature* 434, 590–597. doi.org/10.1038/nature03411
- Sobolev, A. V., Hofmann, A.W., Kuzmin, D. V., Yaxley, G.M., Arndt, N.T., Chung, S.-L., Danyushevsky, L. V., Elliott, T., Frey, F.A., Garcia, M.O., Gurenko, A.A., Kamenetsky, V.S., Kerr, A.C., Krivolutsкая, N.A., Matvienkov, V. V., Nikogosian, I.K., Rocholl, A., Sigurdsson, I.A., Sushchevskaya, N.M., Teklay, M., 2007. The Amount of Recycled Crust in Sources of Mantle-Derived Melts. *Science* 316 (5823), 412–417. doi.org/10.1126/science.1138113
- Staudigel, H., Plank, T., White, B., Schmincke, H.-U., 1996. Geochemical fluxes during seafloor alteration of the basaltic upper oceanic crust: DSDP sites 417 and 418, in: *Subduction Top to Bottom*. pp. 19–38. doi.org/10.1029/GM096p0019
- Steinberger, B., O'Connell, R.J., 1998. Advection of plumes in mantle flow: implications for hotspot motion, mantle viscosity and plume distribution. *Geophys. J. Int.* 132, 412–434. doi.org/10.1046/j.1365-246x.1998.00447.x
- Stracke, A., Bizimis, M., Salters, V.J.M., 2003. Recycling oceanic crust: Quantitative constraints. *Geochemistry, Geophys. Geosystems* 4 (3). 8003 doi.org/10.1029/2001GC000223
- Stracke, A., Hofmann, A.W., Hart, S.R., 2005. FOZO, HIMU, and the rest of the mantle zoo. *Geochemistry, Geophys. Geosystems* 6, Q05007. doi.org/10.1029/2004GC000824
- Stuessy, T.F., Foland, K.A., Sutter, J.F., Sanders, R.W., Silva, M., 1984. Botanical and geological significance of potassium-argon dates from the Juan Fernandez Islands. *Science* 225 (4657), 49–51. doi.org/10.1126/science.225.4657.49
- Sun, S., McDonough, W.F., 1989. Chemical and isotopic systematics of oceanic basalts: implications for mantle composition and processes. *Geol. Soc. London, Spec. Publ.* 42, 313–345. doi.org/10.1144/GSL.SP.1989.042.01.19
- Tassara, A., Götze, H.-J., Schmidt, S., Hackney, R., 2006. Three-dimensional density model of the Nazca plate and the Andean continental margin. *J. Geophys. Res.* 111, B09404. doi.org/10.1029/2005JB003976
- Todd, E., Stracke, A., Scherer, E.E. (2015) Effects of simple acid leaching of crushed and powdered geological materials on high-precision Pb isotope analyses. *Geochemistry, Geophysics, Geosystems* 16, 2276-2302, doi.org/10.1002/2015gc005804
- Trela, J., Vidito, C., Gazel, E., Herzberg, C., Class, C., Whalen, W., Jicha, B., Bizimis, M., Alvarado, G.E., 2015. Recycled crust in the Galápagos Plume source at 70 Ma: Implications for plume evolution. *Earth Planet. Sci. Lett.* 425, 268–277. doi.org/10.1016/j.epsl.2015.05.036

- Truong, T.B., Castillo, P.R., Hilton, D.R., Day, J.M.D., 2018. The trace element and Sr-Nd-Pb isotope geochemistry of Juan Fernandez lavas reveal variable contributions from a high- $^3\text{He}/^4\text{He}$ mantle plume. *Chem. Geol.* 476, 280–291. doi.org/10.1016/j.chemgeo.2017.11.024
- Turner, S.J., Langmuir, C.H., Dungan, M.A., Escrig, S., 2017. The importance of mantle wedge heterogeneity to subduction zone magmatism and the origin of EM1. *Earth Planet. Sci. Lett.* 472, 216–228. doi.org/10.1016/j.epsl.2017.04.051
- von Huene, R., Corvalán, J., Flueh, E.R., Hinz, K., Korstgard, J., Ranero, C.R., Weinrebe, W., 1997. Tectonic control of the subducting Juan Fernández Ridge on the Andean margin near Valparaiso, Chile. *Tectonics* 16, 474–488. doi.org/10.1029/96TC03703
- Weaver, B.L., 1991. The origin of ocean island basalt end-member compositions: trace element and isotopic constraints. *Earth Planet. Sci. Lett.* 104, 381–397. doi.org/10.1016/0012-821X(91)90217-6
- White, W.M., 2015. Isotopes, DUPAL, LLSVPs, and Anekantavada. *Chem. Geol.* 419, 10–28. doi.org/10.1016/j.chemgeo.2015.09.026
- Willbold, M., Stracke, A., 2010. Formation of enriched mantle components by recycling of upper and lower continental crust. *Chem. Geol.* 276, 188–197. doi.org/10.1016/j.chemgeo.2010.06.005
- Workman, R.K., Hart, S.R., 2005. Major and trace element composition of the depleted MORB mantle (DMM). *Earth Planet. Sci. Lett.* 231, 53–72. doi.org/10.1016/j.epsl.2004.12.005
- Yang, Z.-F., Zhou, J.-H., 2013. Can we identify source lithology of basalt? *Sci. Rep.* 3, 1856. doi.org/10.1038/srep01856
- Yaxley, G.M., Green, D.H., 1998. Reactions between eclogite and peridotite: Mantle refertilisation by subduction of oceanic crust. *Schweizerische Mineral. Und Petrogr. Mitteilungen* 78, 243–255.
- Zindler, A., Hart, S., 1986. Chemical Geodynamics. *Annu. Rev. Earth Planet. Sci.* 14, 493–571. doi.org/10.1146/annurev.ea.14.050186.002425

Table 1. Petrography of representative shield samples from the O'Higgins Guyot, Alpha Seamount, Robinson Crusoe Island, and Alejandro Selkirk Island based on the counting of 500 points using JMicroVision 1.2.7 software. Mineralogy is reported as vesicle-free volume percent for phenocrysts and microphenocrysts (> 0.2 mm in diameter). Rock type according mineralogy and chemistry. GM: groundmass, Ves: vesicle content, Ol: olivine, Cpx: clinopyroxene, Plg: plagioclase, Op: opaques.

Sample	Rock type	GM (%)	Mineralogy				Ves (%)	
			Ol	Cpx	Plg	Op		
<i>O'Higgins Guyot</i>								
'olivine-rich'	D10-5	picrite	70	29	-	<1	<1	-
	D10-7	picrite	75	25	-	-	-	<1
'differentiated'	D10-42	alkali basalt	92	7	-	1	-	18
<i>Alpha Seamount</i>								
'differentiated'	D11-03	alkali basalt	98	<1	-	2	-	-
	D11-04	alkali basalt	99	<<1	-	1	-	-
	D11-14	alkali basalt	93	2	4	1	-	4
<i>Robinson Crusoe Island</i>								
'olivine-rich'	LL250711-5	tholeiitic basalt	75	25	<<1	<<1	-	-
	MP270112-5B	picrite	76	24	-	-	-	6
'near-primitive'	JR290513-2	tholeiitic basalt	92	7	-	-	1	-
	JR290513-5	alkali basalt	93	2	3	2	-	3
	LL250711-7	tholeiitic basalt	92	6	1	1	-	5
'differentiated'	JR160913-13	tholeiitic basalt	99	<<1	1	<<1	-	1
	LL220112-3	tholeiitic basalt	94	2	2	2	-	5
	LL240711-1	alkali basalt	98	<1	<<1	2	-	12
	LL250711-1	alkali basalt	64	5	10	21	-	4
	LL250711-9	tholeiitic basalt	98	<1	1	1	-	4
<i>Alejandro Selkirk Island</i>								
'olivine-rich'	JR170913-4	picrite	52	47	<<1	-	1	-
	MF-6	tholeiitic basalt	82	17	<<1	1	-	17
	MF-C2	tholeiitic basalt	64	25	6	5	-	1
'near-primitive'	JR170913-5	tholeiitic basalt	80	13	4	3	-	11
	JR170913-16	tholeiitic basalt	90	6	-	4	-	4
	MF-16	tholeiitic basalt	88	10	-	2	-	17
'differentiated'	JR170913-7	alkali basalt	100	<1	-	<1	-	1
	JR180913-1	trachy-basalt	93	3	<<1	4	-	<1
	LL250112-1	alkali basalt	75	4	<<1	21	-	4
	LL260112-4	alkali basalt	99	<1	-	1	-	1

Table 2. Major element (wt%) and Ni (ppm) concentrations of samples from Alpha Seamount, Robinson Crusoe Island, and Alejandro Selkirk Island. Fe₂O₃^T: total iron as ferric iron. LOI (wt%) is included.

Sample		SiO ₂	TiO ₂	Al ₂ O ₃	Fe ₂ O ₃ ^T	MgO	MnO	CaO	Na ₂ O	K ₂ O	P ₂ O ₅	Ni	LOI	Sum
<i>Det. limit</i>		<i>0.01</i>	<i>0.01</i>	<i>0.01</i>	<i>0.04</i>	<i>0.01</i>	<i>0.01</i>	<i>0.01</i>	<i>0.01</i>	<i>0.01</i>	<i>0.01</i>	<i>0.1</i>	<i>0.1</i>	
<i>Alpha Seamount</i>														
D11-02	Dredged	46.80	3.60	15.02	11.80	5.75	0.17	10.07	3.13	1.02	0.46	48.0	1.8	99.62
D11-03	Dredged	45.28	4.02	16.09	12.37	5.82	0.20	9.32	3.37	1.29	0.59	46.5	1.2	99.55
D11-04	Dredged	45.22	3.72	15.63	12.16	4.64	0.18	10.22	3.53	1.19	0.61	49.3	2.5	99.60
D11-07	Dredged	46.16	4.17	15.41	12.77	5.45	0.15	8.07	3.62	1.32	0.56	25.7	1.9	99.58
D11-08	Dredged	46.09	3.51	15.38	11.71	5.80	0.15	9.74	3.11	1.06	0.51	61.3	2.6	99.66
D11-10	Dredged	45.61	3.73	15.61	12.05	4.97	0.18	9.72	3.58	1.20	0.57	49.1	2.4	99.62
D11-12	Dredged	44.36	3.49	15.08	11.74	5.80	0.17	10.82	3.12	0.97	0.52	47.5	3.5	99.57
D11-14	Dredged	45.62	3.08	15.63	11.33	6.33	0.14	10.99	2.70	0.78	0.53	61.3	2.5	99.63
D11-15	Dredged	44.65	3.16	15.60	11.72	6.15	0.15	10.55	2.64	0.88	0.60	69.1	3.5	99.60
D11-17	Dredged	46.04	3.55	16.11	12.26	5.05	0.23	8.35	3.77	1.41	0.72	94.7	2.1	99.59
BM220588-1	Dredged	45.88	3.75	15.63	12.03	4.91	0.19	9.66	3.49	1.18	0.62	86.0	2.0	99.34
BM220588-2	Dredged	45.16	3.91	15.76	12.40	6.05	0.22	9.62	3.17	1.19	0.59	101.0	1.4	99.47
JF1A-1	Dredged	43.23	3.55	14.28	13.60	7.30	0.24	10.49	2.52	0.85	0.75	196.0	2.7	99.51
<i>Robinson Crusoe Island</i>														
JR260112-1	Dyke	47.05	3.42	14.05	12.83	5.96	0.18	9.42	3.02	0.84	0.42	127.7	2.5	99.69
JR260112-3	Dyke	48.10	3.08	14.36	11.12	6.33	0.23	10.70	3.03	0.65	0.35	67.3	1.7	99.65
JR160913-4	Dyke	48.69	3.69	15.59	10.00	4.01	0.11	10.10	3.03	0.72	0.43	81.0	3.3	99.67
JR160913-6	Dyke	46.09	3.31	14.00	12.51	6.03	0.18	10.55	2.89	0.82	0.40	43.1	2.9	99.68
JR160913-7	Dyke	47.76	3.69	14.73	11.02	5.06	0.16	9.46	3.18	1.08	0.57	41.9	2.9	99.61
LL040213-3	Clast	46.60	3.37	14.64	11.46	6.40	0.13	10.57	2.66	0.87	0.43	70.3	2.5	99.63
LL240711-3	Dyke	46.84	3.47	14.80	12.94	5.14	0.16	9.96	2.82	0.45	0.41	39.8	2.7	99.69
LL240711-4	Dyke	46.36	3.38	15.45	12.32	6.50	0.16	8.36	3.50	1.29	0.68	85.2	1.6	99.60
LL240711-5D	Dyke	46.49	3.39	15.53	12.22	6.25	0.15	8.35	3.46	1.26	0.67	83.9	1.8	99.57
LL240711-7	Dyke	47.84	4.07	14.15	13.00	4.54	0.14	9.01	3.28	1.12	0.56	24.6	2.0	99.71
JR220112-1	Dyke	47.37	3.46	15.20	12.51	6.84	0.16	10.16	3.15	0.74	0.40	64.9	-0.3	99.72
JR140913-1	Dyke	47.73	3.38	15.85	13.59	4.78	0.20	7.09	4.13	1.68	0.77	29.6	0.5	99.70
JR160913-11	Dyke	48.79	2.92	15.97	10.49	4.15	0.15	7.37	4.52	1.87	0.70	26.3	2.7	99.63
JR160913-12	Sill	47.27	3.48	14.73	11.27	6.22	0.15	10.81	3.13	0.96	0.43	48.2	1.2	99.65
MP270112-5A	Dyke	44.53	3.75	15.54	12.86	6.39	0.17	9.87	2.24	0.41	0.42	56.8	3.5	99.68
MP270112-5B	Dyke	42.58	2.50	10.80	13.85	18.64	0.18	6.46	1.47	0.38	0.31	737.4	2.1	99.27
<i>Alejandro Selkirk Island</i>														
LL250112-1	Lava	49.01	3.26	15.48	11.14	5.39	0.15	10.10	3.66	1.22	0.57	43.6	-0.3	99.71
LL250112-2	Lava	48.01	2.52	14.97	12.54	5.91	0.17	10.78	2.91	0.52	0.27	55.5	1.0	99.60
LL260112-1	Lava	46.39	3.25	13.31	12.58	10.29	0.16	8.74	2.99	1.02	0.47	269.4	0.3	99.50
LL260112-2	Lava	47.10	3.72	14.90	13.44	5.87	0.17	9.11	3.25	0.72	0.51	26.5	0.9	99.69
LL260112-4	Lava	49.03	3.43	15.43	11.70	5.51	0.16	9.03	3.53	1.10	0.54	35.6	0.2	99.66
LL270112-1	Lava	47.16	2.90	16.43	11.46	6.30	0.16	10.20	2.74	0.43	0.33	92.4	1.6	99.71
MF-20	Lava	46.47	3.72	14.35	12.55	8.54	0.15	9.36	3.14	1.24	0.55	153.8	-0.6	99.53
MF-C2	Lava	45.69	2.39	12.31	13.95	15.01	0.17	7.03	2.39	0.63	0.37	508.0	-0.6	99.40
MF-6	Lava	46.52	1.95	12.34	12.91	14.42	0.17	8.50	2.24	0.52	0.23	469.8	-0.4	99.44
MF-16	Lava	47.18	2.17	13.44	12.48	11.35	0.16	9.27	2.52	0.58	0.26	326.0	0.1	99.51
MF-3	Lava	43.79	1.82	11.61	13.25	15.92	0.17	7.78	2.70	0.34	0.18	531.0	1.8	99.36
MF-C4	Lava	46.92	2.59	12.99	13.54	12.54	0.17	7.34	2.59	0.75	0.34	375.2	-0.3	99.50
JR170913-1	Lava	48.96	2.80	14.51	11.62	7.05	0.16	11.10	2.56	0.60	0.31	45.8	0.0	99.67
JR170913-5	Lava	46.70	2.46	13.80	11.68	10.70	0.15	9.39	2.53	0.51	0.31	302.6	1.3	99.53
JR170913-4	Cobble	43.84	1.19	6.10	14.55	26.91	0.18	4.28	1.04	0.28	0.13	1298.8	0.6	99.10
JR170913-8	Lava	46.60	3.04	16.04	12.31	7.01	0.16	9.78	2.76	0.33	0.40	111.0	1.2	99.63
JR170913-9	Lava	46.47	2.94	14.94	12.59	7.23	0.16	10.39	2.81	0.47	0.37	106.1	1.2	99.57
JR170913-10	Lava	49.98	2.77	14.71	12.18	5.82	0.17	10.30	2.63	0.59	0.29	21.9	0.3	99.74
JR170913-12	Lava	49.38	3.07	14.01	11.52	5.48	0.19	11.00	2.92	0.85	0.34	28.8	0.9	99.66
JR170913-14	Lava	46.80	2.40	13.86	13.15	10.48	0.17	9.24	2.71	0.54	0.29	248.2	-0.1	99.55
JR170913-16	Lava	47.28	2.89	14.40	11.56	8.88	0.12	8.31	2.97	1.01	0.44	191.2	1.7	99.56
JR170913-18	Lava	46.46	2.80	13.33	12.24	11.33	0.16	9.12	2.77	0.97	0.40	302.5	-0.1	99.49
JR170913-19	Lava	47.99	2.43	14.08	12.50	8.97	0.17	10.04	2.30	0.42	0.20	138.6	0.5	99.60
JR180913-1	Lava	50.33	3.13	16.54	11.59	4.18	0.17	6.60	4.32	1.89	0.92	33.8	0.0	99.67
JR180913-2	Lava	47.17	3.48	17.17	12.48	4.14	0.16	6.03	3.56	1.74	0.88	37.6	2.9	99.71
JR170913-7	Dome	48.78	4.06	14.68	13.39	4.49	0.16	7.84	3.54	1.24	0.62	18.4	0.9	99.70
LL250112-3	Dyke	47.25	3.11	14.22	11.63	5.24	0.15	9.84	3.37	0.91	0.44	45.0	3.5	99.66
LL250112-4	Dyke	48.26	2.96	14.97	11.06	6.02	0.14	10.97	2.86	0.72	0.35	58.4	1.3	99.61
LL270112-2	Dyke	46.32	3.46	13.61	12.62	9.60	0.16	8.83	2.99	1.13	0.54	234.6	0.3	99.56
JR170913-2	Dyke	48.85	3.26	15.29	11.05	5.78	0.15	10.28	3.02	0.94	0.41	48.9	0.6	99.63
JR170913-6	Dyke	48.46	3.32	15.25	11.25	5.59	0.22	10.82	2.95	0.84	0.35	111.1	0.6	99.65
JR170913-11	Dyke	49.06	3.37	15.48	11.21	4.67	0.26	11.11	2.84	0.74	0.34	41.7	0.6	99.68
JR170913-13	Dyke	47.68	3.31	15.05	10.85	6.14	0.14	9.65	2.92	1.00	0.44	66.4	2.5	99.68

ACCEPTED MANUSCRIPT

JR170913-15	Dyke	48.23	2.93	14.97	11.95	5.56	0.17	10.77	2.84	0.69	0.34	36.5	1.2	99.65
JR170913-17	Dyke	48.69	3.41	14.96	11.09	6.80	0.15	10.00	3.09	0.98	0.48	94.3	0.0	99.65
JR170913-20	Dyke	48.55	2.96	14.94	11.71	6.28	0.16	10.68	3.09	0.89	0.39	58.2	0.0	99.65
JR170913-22	Sill	48.77	2.89	15.21	11.63	6.20	0.15	10.76	3.15	0.88	0.39	62.3	-0.4	99.67

ACCEPTED MANUSCRIPT

Table 3. Trace element data (ppm, Cr₂O₃ in wt%) for lavas and dykes from Alpha Seamount, Robinson Crusoe Island, and Alejandro Selkirk Island.

Sample <i>Det. limit</i>	Cr ₂ O ₃ <i>0.002</i>	Sc <i>1</i>	Ba <i>1</i>	Co <i>0.2</i>	Ga <i>0.5</i>	Hf <i>0.1</i>	Nb <i>0.1</i>	Rb <i>0.1</i>	Sr <i>0.5</i>	Ta <i>0.1</i>	Th <i>0.2</i>	U <i>0.1</i>	V <i>8</i>	Zr <i>0.1</i>	Y <i>0.1</i>
<i>Alpha Seamount</i>															
D11-02	0.014	27	273	58.2	27.2	6.9	45.3	22.3	639.3	2.9	3.4	0.9	416	289.3	35.6
D11-03	0.003	19	369	61.9	28.8	7.5	60.1	30.2	902.8	3.7	4.1	1.2	379	338.9	35.5
D11-04	0.016	24	310	50.5	27.7	8.0	54.8	27.3	957.7	3.4	4.2	1.2	402	345.1	43.1
D11-07	0.007	22	317	46.2	29.3	8.5	57.8	32.0	670.0	3.7	4.3	1.1	400	386.8	43.2
D11-08	0.021	25	255	51.1	25.5	7.1	45.5	19.7	664.1	2.9	3.5	0.5	373	297.1	36.0
D11-10	0.016	24	298	49.7	26.8	7.6	52.0	26.1	824.9	3.3	4.0	1.0	377	350.1	39.4
D11-12	0.017	28	246	55.0	27.0	6.4	41.9	21.0	637.4	2.8	3.2	1.4	400	277.3	32.1
D11-14	0.037	31	197	45.9	24.9	6.2	34.0	11.0	587.5	2.3	2.5	1.5	396	238.6	31.7
D11-15	0.037	31	191	44.8	24.0	6.5	35.4	12.1	667.6	2.3	2.7	1.7	395	242.6	37.8
D11-17	0.018	21	364	62.5	28.4	8.6	64.4	34.6	762.5	4.1	5.2	1.6	368	400.5	44.4
BM220588-1	0.018	24	231	49.4	21.7	6.6	41.2	20.7	609.7	2.6	3.3	1.2	293	275.7	32.7
BM220588-2	0.011	21	267	60.5	21.1	6.5	44.2	21.7	627.5	2.7	3.2	1.0	307	253.2	29.5
JF1A-1	0.020	29	193	63.6	22.0	5.7	36.2	11.8	966.2	2.4	2.6	1.4	346	233.4	29.1
<i>Robinson Crusoe Island</i>															
LL230711-7	0.008	27	127	36.6	21.0	5.0	32.1	5.4	514.8	2.2	2.3	0.6	378	205.5	28.4
LL230112-1	0.032	24	336	54.7	29.7	7.8	56.5	27.4	787.7	3.4	4.2	1.1	434	332.8	38.1
JR260112-1	0.010	28	512	33.3	22.3	5.2	35.8	13.4	454.8	2.2	2.4	0.7	319	207.7	27.8
JR260112-3	0.034	29	202	44.7	19.7	5.2	27.7	12.0	444.8	1.7	2.1	0.6	287	198.1	32.6
JR160913-4	0.020	30	249	35.6	24.5	6.4	37.8	6.4	576.3	2.6	3.0	0.9	298	255	42.6
JR160913-6	0.013	28	211	42.4	20.7	5.2	33.9	15.0	513.7	2.0	2.9	0.7	313	222.8	29.0
JR160913-7	0.018	26	233	42.5	22.7	7.1	41.5	18.9	549.6	2.8	3.5	1.1	310	298	32.1
JR300513-3	0.030	28	212	44.1	21.7	5.8	36.2	20.0	472.1	2.3	3.0	0.7	299	233.1	28.5
LL040213-3	0.032	26	211	42.8	23.5	5.9	33.4	11.3	527.8	2.1	2.8	0.3	312	236.4	29.4
JR290513-5	0.066	25	245	46.7	17.8	4.5	35.4	29.0	634.1	2.3	2.8	0.6	301	203.7	24.5
LL240711-1	0.012	28	242	42.5	22.0	5.5	38.7	19.7	564.0	2.4	3.1	0.7	369	231	31.5
LL240711-2	0.030	29	221	43.2	20.3	4.8	34.5	15.9	535.2	2.2	2.7	0.6	344	188.7	26.4
LL240711-6	0.021	25	239	42.3	22.7	5.6	36.7	16.0	608.8	2.4	2.9	0.7	351	217.2	43.3
LL260711-2	0.010	27	229	43.2	23.5	6.2	39.3	20.1	586.6	2.5	2.8	0.8	385	230.1	30.1
JR270513-2	0.130	21	199	71.7	15.7	4.2	30.1	16.3	412.3	1.9	2.4	0.4	286	195.8	24.3
JR270513-1	0.018	27	320	41.0	24.4	6.4	44.5	12.8	584.3	2.8	3.7	0.8	354	257.7	35.1
JR290513-2	0.187	25	177	59.5	15.5	3.6	20.7	12.4	416.6	1.3	1.7	0.4	264	145.6	18.3
LL250711-1	0.038	25	345	39.2	23.1	6.7	46.3	16.6	738.8	3.0	3.6	0.6	345	258.1	30.9
LL250711-3	0.028	25	307	43.9	24.7	6.9	47.0	19.7	707.4	3.0	3.4	0.5	370	274.2	49.9
LL250711-5	0.145	20	75	88.1	15.0	2.5	13.0	7.3	267.2	0.9	0.9	0.3	243	102.8	17.7
LL250711-7	0.075	28	197	50.9	20.5	4.7	29.7	7.7	486.3	1.8	2.2	0.3	343	176	28.9
LL220112-2	0.014	30	254	34.5	23.1	6.5	38.4	13.9	518.8	2.4	2.9	0.5	298	244.3	38.7
LL220112-3	0.041	30	196	39.8	19.8	5.4	33.3	15.1	495.6	2.1	2.1	0.5	313	211.5	26.6
LL220112-5	0.004	23	334	57.5	32.5	9.6	61.3	36.0	850.0	3.5	4.6	1.2	435	375.3	46.1
JR220112-2	0.007	25	227	37.9	22.9	5.3	40.4	21.5	544.8	2.4	2.8	0.7	299	223.5	25.1
JR250513-1	0.242	18	235	118.6	11.6	3.1	18.3	10.2	248.6	1.0	1.3	0.4	183	128.2	17.5
JR250513-2	0.019	29	225	44.0	19.2	4.2	26.2	11.9	454.8	1.6	2.0	0.5	292	170.3	27.7
JR250513-4	0.027	29	221	37.9	20.1	5.2	30.7	13.8	520.7	1.8	2.4	0.5	291	200.7	25.2
JR250513-5	0.019	21	309	34.1	21.3	6.4	46.5	23.5	689.9	2.8	3.9	0.9	309	278.7	29.6
JR160913-1	0.044	31	3789	45.5	22.2	5.6	33.3	7.2	751.1	2.1	3.3	0.5	277	226.4	37.6
JR160913-10	0.050	30	176	34.3	22.1	5.4	30.6	19.8	542.3	1.9	2.6	0.7	313	212.8	27.0
JR160913-13	0.028	29	223	36.4	21.7	5.8	40.9	16.2	613.3	2.6	3.6	0.7	319	238.4	29.0
LL240711-3	0.010	29	190	38.2	22.5	5.5	29.5	2.5	469.1	1.8	2.3	0.3	356	206.7	31.2
LL240711-4	0.027	18	352	43.8	22.7	7.8	50.6	40.3	704.0	3.2	4.1	1.1	256	308	31.1
LL240711-5D	0.024	18	329	42.4	22.0	7.4	51.8	35.6	693.3	3.2	4.4	1.2	262	313	33.7
LL240711-7	0.003	27	233	34.1	23.0	6.8	41.9	21.7	526.9	2.7	3.1	0.7	405	272	32.8
JR220112-1	0.032	25	161	37.1	21.0	4.9	27.5	14.4	492.9	1.8	2.1	0.4	267	193.3	26.1
JR140913-1	0.006	19	334	34.9	26.2	8.3	53.6	28.7	556.7	3.0	4.8	0.6	303	364.3	38.6
JR160913-11	0.007	15	355	28.6	26.6	9.5	60.6	40.0	563.3	3.6	6.0	1.6	216	424.2	37.8
JR160913-12	0.025	29	220	40.8	21.7	5.6	39.3	19.1	554.4	2.4	3.4	0.8	325	231	27.2
LL250711-8	0.017	29	253	48.4	22.2	6.0	38.8	17.4	539.5	2.5	2.5	0.6	379	230.8	26.8
LL250711-9	0.019	30	222	47.3	23.0	5.1	36.2	17.2	524.8	2.2	2.6	0.7	378	202.9	32.4
LL040213-2	0.130	23	143	72.3	17.7	3.6	23.8	12.0	370.8	1.4	1.7	0.2	267	161.3	20.9
LL300113-1	0.071	28	162	54.7	19.6	4.0	26.9	11.0	393.5	1.4	1.8	0.2	305	176.5	22.0
LL250711-4	0.027	25	275	47.7	23.6	7.6	44.8	18.0	590.0	2.9	3.5	0.8	330	277.5	36.5
MP270112-4	0.023	21	270	42.3	21.1	7.1	40.4	23.7	640.4	2.8	3.1	0.9	256	274.4	30.7
MP270112-5A	0.026	31	196	43.0	21.8	6.2	37.2	2.4	454.6	2.1	2.4	0.1	343	228.3	23.9
MP270112-5B	0.151	23	156	81.6	16.4	3.7	25.1	3.0	261.5	1.6	1.6	0.2	228	160.1	16.3
<i>Alejandro Selkirk Island</i>															
LL250112-1	0.020	22	268	32.8	22.5	7.1	37.2	26.3	680.2	2.3	3.6	0.8	228	283.5	26.8

LL250112-2	0.035	28	166	58.5	26.5	6.1	29.5	15.5	515.1	1.7	2.7	0.5	373	217.8	34.6
LL260112-1	0.063	21	214	51.1	19.7	6.4	32.7	19.2	560.5	2.1	2.8	0.8	216	258.1	25.3
LL260112-2	0.007	25	216	40.2	23.8	6.7	31.4	6.2	472.1	1.9	2.8	0.5	240	262.7	32.1
LL260112-4	0.020	23	212	37.1	24.4	7.3	30.6	16.5	561.7	2.1	2.8	0.8	214	299.6	29.6
LL270112-1	0.050	27	132	37.4	21.7	4.6	20.5	1.9	471.5	1.4	1.9	0.1	229	194.6	24.4
MF-20	0.047	21	306	58.3	26.6	8.6	43.6	28.3	820.1	2.9	3.6	0.9	291	367.4	30.6
MF-C2	0.104	18	149	85.6	21.8	6.7	25.9	8.4	430.8	1.6	2.6	0.6	194	259.8	30.0
MF-6	0.110	22	108	81.5	19.4	4.4	17.9	11.5	406.4	1.1	1.4	0.4	240	178.8	23.8
MF-16	0.081	25	119	69.2	21.4	4.3	19.4	12.7	446.2	1.2	1.5	0.5	265	194.8	27.1
MF-3	0.129	22	116	97.1	18.7	4.5	16.4	6.4	363.2	1.1	1.8	0.4	226	185	22.2
MF-C4	0.079	19	184	78.8	23.4	6.7	24.5	19.2	430.1	1.8	2.5	0.8	216	289.1	35.2
JR170913-1	0.037	30	145	44.2	20.3	4.6	23.4	12.3	474.9	1.5	2.2	0.5	278	189.6	26.0
JR170913-5	0.097	24	181	57.0	18.6	4.7	25.4	9.8	481.5	1.7	2.4	0.4	219	184	22.8
JR170913-4	0.229	14	67	120.5	9.8	2.0	11.4	6.6	181.2	0.6	1.1	0.3	129	81.3	11.1
JR170913-8	0.047	26	158	45.4	22.5	5.8	24.8	1.6	486.8	1.6	2.2	0.4	247	236	28.8
JR170913-9	0.051	27	147	45.7	21.8	5.7	24.9	4.7	512.1	1.7	2.2	0.4	272	223.5	28.4
JR170913-10	0.029	29	110	40.0	20.8	4.8	20.6	11.3	399.8	1.4	1.9	0.4	277	179.9	27.9
JR170913-12	0.021	29	168	40.1	21.6	5.4	26.6	18.7	425.6	1.7	2.7	0.7	284	209.7	30.3
JR170913-14	0.083	23	118	61.3	20.4	4.4	18.2	9.5	416.2	1.2	1.7	0.4	227	182.1	24.6
JR170913-16	0.048	19	179	49.4	20.4	6.4	28.4	24.1	552.0	1.8	2.6	0.7	202	251.2	24.6
JR170913-18	0.083	24	226	57.7	21.0	5.5	28.7	21.4	523.7	1.7	2.6	0.8	240	247.8	25.1
JR170913-19	0.065	28	97	53.0	21.4	4.5	19.2	9.2	375.2	1.3	1.6	0.4	258	172.4	25.3
JR180913-1	0.004	16	351	27.1	26.0	9.7	45.9	39.4	524.9	3.0	5.6	1.5	202	432	45.6
JR180913-2	0.008	17	320	33.9	28.6	10.3	46.9	30.2	402.6	3.0	5.1	1.2	224	445	40.3
JR170913-7	0.008	24	218	36.2	25.8	9.0	36.7	26.2	497.6	2.1	3.7	0.9	285	369.9	53.9
LL250112-3	0.023	27	180	37.5	19.6	6.5	29.3	15.3	462.8	1.9	2.6	0.5	247	233.1	30.0
LL250112-4	0.034	28	216	52.2	27.8	7.3	34.6	25.3	672.8	2.2	3.0	0.8	381	280.9	39.1
LL270112-2	0.060	22	218	50.6	20.3	7.2	34.8	27.9	605.7	2.1	2.9	0.5	227	283.4	29.3
JR170913-2	0.030	27	164	36.2	22.0	6.0	25.8	17.5	506.8	1.8	2.3	0.7	272	246.8	30.5
JR170913-6	0.036	27	146	47.2	21.8	5.5	24.7	16.2	517.2	1.5	2.2	0.8	285	216.2	28.1
JR170913-11	0.034	30	135	42.8	22.4	5.7	23.5	14.2	501.7	1.7	1.9	1.1	291	212.9	28.4
JR170913-13	0.030	26	213	37.5	21.0	6.6	31.4	30.6	536.4	2.1	2.7	0.6	267	257.3	29.9
JR170913-15	0.022	27	149	41.3	21.0	5.3	23.8	11.6	483.3	1.6	2.2	0.6	268	209.7	28.6
JR170913-17	0.044	26	191	38.7	23.7	6.8	31.7	21.3	552.2	1.8	2.6	0.7	263	278.2	29.8
JR170913-20	0.031	27	194	42.6	23.8	5.8	29.2	18.2	567.9	1.8	2.6	0.5	262	236.4	27.8
JR170913-22	0.033	27	218	41.5	22.5	5.6	27.5	14.9	573.9	2.0	2.6	0.4	262	223.4	25.0

Table 3. (continued)

Sample <i>Det. limit</i>	Pb <i>0.1</i>	La <i>0.1</i>	Ce <i>0.1</i>	Pr <i>0.02</i>	Nd <i>0.3</i>	Sm <i>0.05</i>	Eu <i>0.02</i>	Gd <i>0.05</i>	Tb <i>0.01</i>	Dy <i>0.05</i>	Ho <i>0.02</i>	Er <i>0.03</i>	Tm <i>0.01</i>	Yb <i>0.05</i>	Lu <i>0.01</i>
<i>Alpha</i>															
<i>Seamount</i>															
D11-02	1.9	34.4	74.2	9.46	41.1	9.28	3.01	9.54	1.32	7.59	1.24	3.34	0.46	2.88	0.37
D11-03	2.9	43.6	91.5	11.51	48.6	10.69	3.40	10.50	1.34	7.94	1.30	3.41	0.44	2.91	0.40
D11-04	1.6	41.3	92.0	11.47	49.1	10.83	3.43	11.01	1.50	8.56	1.49	3.94	0.54	3.53	0.46
D11-07	0.7	44.6	96.6	12.28	49.8	11.51	3.65	11.72	1.53	9.22	1.53	4.00	0.53	3.61	0.45
D11-08	2.3	36.5	75.0	9.55	43.0	9.30	3.11	9.89	1.30	7.55	1.30	3.32	0.44	2.88	0.39
D11-10	1.4	42.4	87.1	11.15	48.0	10.55	3.40	11.09	1.42	8.65	1.38	3.86	0.50	3.47	0.41
D11-12	2.4	32.7	71.9	9.11	39.2	9.02	2.94	9.45	1.27	7.35	1.19	3.18	0.43	2.69	0.37
D11-14	1.0	25.8	58.9	7.73	34.7	7.81	2.64	8.54	1.15	7.13	1.21	3.13	0.41	2.36	0.34
D11-15	1.2	34.1	73.2	9.56	45.0	9.78	3.10	10.24	1.36	8.15	1.39	3.69	0.49	2.88	0.41
D11-17	2.5	49.5	105.7	13.33	57.3	12.31	3.86	12.35	1.63	9.61	1.63	4.39	0.54	3.99	0.50
BM220588-1		34.3	73.3	9.19	38.5	8.47	2.84	8.40	1.24	6.86	1.22	3.34	0.43	2.77	0.38
BM220588-2		33.1	70.4	9.04	37.9	7.94	2.69	8.02	1.14	6.21	1.16	3.05	0.38	2.26	0.33
JF1A-1		26.5	56.0	7.72	33.6	7.13	2.32	7.55	1.08	6.00	1.15	3.05	0.38	2.35	0.33
<i>Robinson Crusoe Island</i>															
LL230711-7	1.6	25.9	54.8	6.97	29.3	6.90	2.28	6.93	1.11	5.57	1.10	2.93	0.39	2.37	0.32
LL230112-1	0.8	43.2	91.0	11.44	50.4	10.69	3.54	11.32	1.41	8.70	1.31	3.40	0.45	2.51	0.36
JR260112-1	0.7	25.6	53.4	6.86	29.5	6.70	2.26	7.25	1.11	5.97	1.03	2.89	0.42	2.38	0.36
JR260112-3	0.4	26.0	50.0	7.11	32.8	7.53	2.45	7.51	1.23	6.47	1.20	3.18	0.44	2.60	0.34
JR160913-4	1.4	33.3	60.7	9.12	39.5	9.37	3.18	9.68	1.47	7.92	1.62	4.14	0.55	3.43	0.48
JR160913-6	1.0	28.0	56.9	7.44	30.6	6.94	2.25	6.83	1.09	6.09	1.07	2.71	0.39	2.24	0.32
JR160913-7	0.7	35.1	75.3	9.62	41.2	8.85	2.90	9.03	1.35	7.05	1.31	3.34	0.42	2.47	0.37
JR300513-3	1.4	30.9	63.9	8.35	35.9	7.80	2.53	7.52	1.12	6.30	1.18	2.98	0.40	2.36	0.32
LL040213-3	0.5	27.3	60.4	8.02	34.3	7.54	2.51	7.62	1.11	6.49	1.17	2.81	0.38	2.41	0.33
JR290513-5	1.0	28.0	59.3	7.56	30.6	6.39	2.13	6.25	0.97	5.35	0.95	2.39	0.33	1.87	0.26
LL240711-1	0.5	32.1	67.6	8.92	38.4	8.15	2.72	8.14	1.28	6.44	1.24	3.11	0.44	2.47	0.33
LL240711-2	0.8	27.8	57.6	7.07	29.6	6.63	2.24	6.59	1.05	5.39	1.04	2.71	0.38	2.27	0.30
LL240711-6	24.2	34.8	69.6	9.23	42.0	8.98	3.05	9.84	1.52	7.71	1.58	4.09	0.56	3.20	0.44
LL260711-2	0.5	30.6	65.5	8.27	36.0	7.77	2.56	7.74	1.22	5.97	1.20	3.11	0.42	2.45	0.34
JR270513-2	0.9	24.1	51.5	6.80	27.2	6.19	1.99	6.17	0.95	5.30	0.89	2.25	0.30	1.71	0.25
JR270513-1	2.2	38.7	70.6	10.11	42.8	8.82	2.90	8.63	1.29	6.85	1.26	3.22	0.42	2.33	0.33
JR290513-2	0.6	18.0	38.5	4.88	20.8	4.75	1.55	4.83	0.78	4.12	0.70	1.74	0.25	1.50	0.20
LL250711-1	1.9	36.2	75.0	9.78	42.6	9.00	2.98	8.57	1.33	6.21	1.16	2.94	0.37	2.15	0.30
LL250711-3	1.0	38.8	77.7	10.90	48.8	10.84	3.67	11.24	1.81	9.04	1.83	4.65	0.64	3.67	0.51
LL250711-5	0.3	9.8	22.8	3.17	15.3	3.71	1.22	3.91	0.65	3.42	0.67	1.82	0.25	1.45	0.21
LL250711-7	0.4	24.6	52.2	6.86	30.0	6.83	2.25	6.90	1.15	5.62	1.11	2.82	0.42	2.46	0.34
LL220112-2	0.5	41.6	85.8	11.36	48.6	10.57	3.44	10.36	1.53	8.58	1.46	3.69	0.48	2.73	0.37
LL220112-3	0.5	27.0	57.0	7.74	31.4	7.48	2.41	7.57	1.12	6.29	1.15	2.79	0.39	2.33	0.31
LL220112-5	1.2	44.4	96.1	12.21	53.1	11.52	3.84	12.07	1.60	9.26	1.62	4.44	0.58	3.39	0.47
JR220112-2	0.9	29.3	59.9	7.72	32.9	7.08	2.26	6.83	1.04	5.53	0.97	2.61	0.37	2.00	0.28
JR250513-1	0.7	17.8	34.3	4.76	19.9	4.24	1.49	4.56	0.67	3.64	0.63	1.52	0.21	1.32	0.21
JR250513-2	0.9	22.4	47.7	6.46	26.9	6.06	2.06	6.52	0.99	5.42	1.00	2.63	0.36	2.06	0.30
JR250513-4	0.7	24.9	52.4	6.84	28.4	6.23	2.12	6.74	0.99	5.44	0.94	2.49	0.35	1.98	0.28
JR250513-5	0.8	38.3	81.1	10.01	39.4	8.42	2.68	7.90	1.24	6.42	1.11	2.90	0.38	2.25	0.31
JR160913-1	1.1	49.6	85.5	13.34	56.1	12.15	3.73	11.23	1.63	8.92	1.57	3.79	0.51	2.78	0.38
JR160913-10	0.7	25.6	54.2	6.97	31.9	6.89	2.34	7.22	1.03	5.69	1.00	2.65	0.37	2.24	0.31
JR160913-13	0.8	32.3	65.7	8.33	34.8	7.26	2.47	7.43	1.12	6.12	1.09	2.79	0.40	2.41	0.33
LL240711-3	1.4	24.6	50.9	7.01	30.7	7.10	2.36	7.31	1.17	5.93	1.16	2.99	0.43	2.40	0.35
LL240711-4	1.5	42.0	86.2	10.48	42.9	9.03	2.83	8.23	1.25	6.07	1.17	2.89	0.41	2.41	0.33
LL240711-5D	1.6	41.9	87.6	10.71	43.9	9.04	2.92	8.60	1.32	6.68	1.26	3.23	0.44	2.55	0.37
LL240711-7	1.6	31.2	67.1	8.94	38.3	8.59	2.80	8.46	1.33	6.76	1.30	3.34	0.47	2.66	0.39
JR220112-1	0.4	22.0	47.2	6.02	26.7	6.45	2.21	6.51	1.01	5.15	1.00	2.75	0.34	2.22	0.34
JR140913-1	1.7	44.2	96.7	12.56	51.9	11.02	3.63	10.80	1.60	8.62	1.59	3.84	0.52	3.10	0.43
JR160913-11	2.4	50.9	103.3	12.95	52.3	10.66	3.45	9.96	1.48	7.88	1.47	3.69	0.53	3.11	0.45
JR160913-12	0.9	32.3	68.5	8.38	34.6	7.53	2.48	7.06	1.14	6.10	1.08	2.80	0.38	2.16	0.33
LL250711-8	1.1	29.3	64.4	8.05	34.0	7.64	2.53	7.10	1.15	5.66	1.05	2.67	0.37	2.16	0.30
LL250711-9	1.3	31.6	59.2	8.09	34.2	7.72	2.59	7.49	1.24	6.29	1.25	3.26	0.45	2.61	0.37
LL040213-2	0.6	19.1	40.5	5.40	22.9	5.24	1.82	5.32	0.77	4.45	0.83	1.98	0.27	1.59	0.24
LL300113-1	0.6	20.3	45.0	5.86	26.7	5.43	1.97	5.80	0.82	5.40	0.84	2.13	0.31	1.48	0.25
LL250711-4	0.5	35.9	75.9	9.68	40.6	8.86	2.90	8.62	1.40	6.94	1.41	3.67	0.50	2.95	0.42
MP270112-4	1.2	36.0	72.0	9.67	42.5	8.72	2.92	8.90	1.31	7.21	1.31	3.16	0.44	2.57	0.34
MP270112-5A	1.3	20.4	49.4	6.40	29.5	6.86	2.31	6.63	0.99	5.44	1.15	2.57	0.29	2.15	0.25
MP270112-5B	0.6	14.8	34.3	4.40	20.7	4.38	1.49	4.48	0.68	4.16	0.73	1.73	0.21	1.36	0.19
<i>Alejandro Selkirk Island</i>															
LL250112-1	1.7	35.9	74.8	9.27	38.2	8.56	2.76	8.38	1.20	6.21	1.07	2.82	0.35	2.04	0.29
LL250112-2	0.5	24.9	52.6	6.93	30.8	7.43	2.67	8.43	1.20	7.16	1.18	3.30	0.46	3.11	0.39
LL260112-1	1.1	28.8	60.8	8.13	34.5	8.05	2.59	8.29	1.13	6.14	1.06	2.54	0.36	1.97	0.27

LL260112-2	0.6	28.4	61.1	8.26	36.3	8.58	2.78	9.08	1.32	7.60	1.29	3.18	0.40	2.62	0.34
LL260112-4	0.5	31.9	71.4	9.50	39.3	9.25	3.11	9.01	1.34	7.60	1.24	3.11	0.40	2.33	0.31
LL270112-1	0.5	18.1	42.5	5.50	27.8	6.13	2.21	7.00	1.00	4.99	0.94	2.50	0.32	2.01	0.32
MF-20	1.1	38.0	85.2	11.01	50.5	11.06	3.65	10.71	1.39	7.32	1.14	2.81	0.33	2.05	0.24
MF-C2	0.5	22.7	50.5	6.89	30.2	7.60	2.43	8.05	1.12	6.26	1.04	2.94	0.36	2.19	0.29
MF-6	<0,1	15.7	35.2	4.90	23.8	5.59	1.86	6.00	0.85	5.03	0.94	2.42	0.31	1.84	0.25
MF-16	0.1	17.6	40.0	5.42	24.4	6.17	2.08	7.11	0.99	5.60	0.98	2.82	0.35	2.39	0.30
MF-3	0.7	17.2	37.8	5.24	23.5	5.79	1.92	6.39	0.88	5.17	0.82	2.19	0.31	1.71	0.24
MF-C4	0.3	25.1	55.2	7.59	34.6	8.59	2.78	9.20	1.28	7.03	1.26	3.28	0.44	2.47	0.33
JR170913-1	0.4	20.9	45.6	5.96	26.9	6.32	2.16	6.55	0.98	5.49	0.99	2.66	0.37	2.24	0.31
JR170913-5	0.9	23.5	46.5	5.91	24.7	5.67	1.94	5.69	0.88	4.83	0.88	2.28	0.31	1.76	0.25
JR170913-4	0.4	9.5	20.1	2.63	12.2	2.66	0.91	2.64	0.40	2.36	0.42	1.06	0.15	0.87	0.13
JR170913-8	1.1	25.5	52.7	8.26	37.4	8.46	2.90	8.26	1.31	7.25	1.19	3.02	0.38	2.24	0.31
JR170913-9	0.9	22.5	49.2	6.72	29.7	6.91	2.38	7.44	1.09	6.11	1.09	2.70	0.39	2.27	0.33
JR170913-10	0.4	18.6	39.4	5.31	23.8	6.06	2.04	6.32	1.02	5.76	1.09	2.80	0.38	2.20	0.33
JR170913-12	0.4	24.2	51.1	6.56	29.3	6.80	2.34	7.26	1.18	6.93	1.23	3.24	0.44	2.61	0.36
JR170913-14	0.4	16.9	37.7	5.00	22.4	5.49	1.99	5.92	0.93	5.00	0.95	2.37	0.34	2.01	0.27
JR170913-16	0.8	26.0	55.9	7.49	33.2	7.58	2.52	7.02	1.14	5.60	0.96	2.30	0.30	1.75	0.26
JR170913-18	0.6	26.9	57.6	7.47	32.9	7.10	2.17	6.43	1.03	5.34	0.98	2.32	0.32	1.92	0.28
JR170913-19	0.5	15.6	35.8	4.60	20.4	5.25	1.80	5.70	0.97	5.23	0.95	2.49	0.33	2.06	0.31
JR180913-1	26.0	53.9	106.9	14.88	62.1	13.30	4.16	12.81	1.92	10.34	1.76	4.55	0.63	3.73	0.48
JR180913-2	2.4	46.7	101.0	12.93	55.7	12.18	3.86	12.20	1.75	9.11	1.53	4.00	0.56	3.22	0.43
JR170913-7	1.0	45.2	84.9	13.98	61.7	14.69	4.74	14.27	2.19	11.87	2.04	5.38	0.73	4.32	0.60
LL250112-3	1.1	27.3	57.4	7.16	33.3	7.08	2.36	7.79	1.16	6.16	1.16	3.06	0.40	2.44	0.34
LL250112-4	0.8	30.1	68.2	8.71	39.9	9.38	3.08	10.17	1.36	8.03	1.28	3.49	0.47	3.02	0.40
LL270112-2	1.5	31.5	67.5	9.03	36.9	8.62	2.80	8.69	1.21	6.58	1.15	2.44	0.32	1.91	0.26
JR170913-2	0.3	23.2	51.6	6.85	31.3	7.17	2.46	7.43	1.22	6.54	1.20	3.09	0.41	2.35	0.35
JR170913-6	0.5	22.2	46.8	6.25	27.7	6.95	2.33	7.07	1.08	5.96	1.04	2.76	0.36	2.23	0.32
JR170913-11	0.3	20.7	45.1	6.12	27.5	6.57	2.25	7.33	1.17	6.43	1.09	2.93	0.40	2.44	0.34
JR170913-13	1.0	27.5	60.7	7.79	34.1	7.86	2.63	7.75	1.25	6.77	1.16	2.86	0.40	2.43	0.36
JR170913-15	1.0	21.8	47.9	6.31	29.1	6.83	2.38	7.14	1.13	6.24	1.12	2.90	0.40	2.32	0.32
JR170913-17	1.2	27.9	63.2	8.34	35.3	8.35	2.61	7.84	1.27	6.68	1.21	2.83	0.39	2.35	0.34
JR170913-20	0.9	25.7	54.9	7.33	31.6	7.26	2.43	7.23	1.10	5.92	1.02	2.82	0.36	2.20	0.32
JR170913-22	1.3	25.8	54.7	7.14	31.7	6.95	2.25	6.70	1.11	5.91	1.04	2.59	0.34	1.97	0.30

Table 4. Radiogenic isotopic compositions of whole-rock representative samples from the shield-stage of the O'Higgins Guyot, Alpha Seamount, Robinson Crusoe Island, and Alejandro Selkirk Island. Standard error (2σ) and laboratory of analysis are indicated (a: GEOMAR Helmholtz Centre, Kiel, Germany; b: Laboratoire Magmas and Volcans, Clermont-Ferrand, France).

Sample	$^{87}\text{Sr}/^{86}\text{Sr}$	\pm	$^{143}\text{Nd}/^{144}\text{Nd}$	\pm	$^{206}\text{Pb}/^{204}\text{Pb}$	\pm	$^{207}\text{Pb}/^{204}\text{Pb}$	\pm	$^{208}\text{Pb}/^{204}\text{Pb}$	\pm	Lab
<i>O'Higgins Guyot</i>											
D10-5	-	-	0.512885	7	-	-	-	-	-	-	b)
D10-7	0.703496	5	0.512899	4	19.0957	8	15.6059	9	38.9466	30	a)
<i>Alpha Seamount</i>											
D11-04	0.703522	5	0.512864	4	19.2218	13	15.6100	11	39.0569	31	a)
D11-14	0.703595	4	0.512848	5	19.2211	13	15.6064	12	39.0652	38	a)
D11-14 rep	0.703590	5	0.512846	4	19.2213	16	15.6064	16	39.0641	34	a)
<i>Robinson Crusoe Island</i>											
LL230711-7	0.703612	8	0.512843	5	-	-	-	-	-	-	b)
LL230711-6	0.703693	6	0.512830	6	-	-	-	-	-	-	b)
JR290513-5	0.703676	5	0.512825	4	19.1698	14	15.6078	12	39.0166	31	a)
MP260112-1	0.703693	5	0.512821	5	19.2607	9	15.6110	8	39.1346	21	a)
JR290513-2	0.703520	5	0.512858	5	19.1667	11	15.6016	9	38.9915	23	a)
LL250711-5	0.703508	4	0.512843	4	19.2874	8	15.6126	7	39.1133	18	a)
LL250711-5 rep	0.703516	5	0.512848	3	-	-	-	-	-	-	a)
LL250711-5 *	0.703564	8	0.512842	6	-	-	-	-	-	-	b)
JR220112-2	0.703616	4	0.512844	3	19.1639	7	15.6023	8	39.0122	26	a)
JR220112-2 *	0.703632	6	0.512836	6	-	-	-	-	-	-	b)
JR220112-1	0.703648	6	0.512823	3	19.1820	11	15.6045	9	39.0558	25	a)
JR220112-1 *	0.703647	5	0.512815	6	-	-	-	-	-	-	b)
LL250711-8	0.703567	4	0.512858	4	19.1680	11	15.6045	9	39.0033	23	a)
LL250711-9	0.703684	6	0.512827	6	-	-	-	-	-	-	b)
LL250711-4	0.703759	7	0.512811	6	-	-	-	-	-	-	b)
MP270112-4	0.703714	6	0.512815	6	-	-	-	-	-	-	b)
<i>Alejandro Selkirk Island</i>											
LL250112-1	0.703596	5	0.512832	5	-	-	-	-	-	-	b)
LL260112-4	0.703577	4	0.512880	4	19.1602	10	15.6093	11	39.0245	31	a)
LL260112-4 *	0.703594	5	0.512870	5	-	-	-	-	-	-	b)
MF-6	0.703582	5	0.512875	4	19.0635	17	15.6071	14	38.9350	37	a)
JR170913-16	0.703667	4	0.512872	5	19.0499	9	15.6075	8	38.9592	22	a)
JR170913-21	0.703561	5	0.512888	4	19.1104	11	15.6086	9	39.0102	26	a)
JR180913-1	0.703663	4	0.512864	4	19.0893	6	15.6091	7	39.0008	22	a)

Table 5. Major (wt%) and trace element (ppm) compositions of primary melts obtained using the PRIMACALC2 model (Kimura and Ariskin, 2014) for parental samples of the Robinson Crusoe and Alejandro Selkirk Islands.

Sample	Robinson Crusoe		Alejandro Selkirk	
	LL040213-2	LL250711-7	MF-3	MF-6
SiO ₂ (wt%)	47.50	47.03	45.46	47.20
TiO ₂	2.51	2.67	1.88	1.97
Al ₂ O ₃	11.27	12.07	11.96	12.47
FeO ^T	11.49	12.02	12.37	11.79
MgO	15.39	14.09	16.82	14.78
MnO	0.18	0.15	0.18	0.18
CaO	8.74	8.75	8.02	8.59
Na ₂ O	2.05	2.34	2.78	2.27
K ₂ O	0.59	0.57	0.35	0.53
P ₂ O ₅	0.28	0.30	0.19	0.23
K (ppm)	4795	4600	2836	4282
Ni	632	815	594	498
Ba	138.78	164.70	113.71	106.93
Hf	3.49	3.93	4.41	4.36
Nb	23.10	24.83	16.08	17.72
Rb	11.65	6.44	6.27	11.39
Sr	360	407	356	402
Ta	1.36	1.50	1.08	1.09
Th	1.65	1.84	1.76	1.39
U	0.19	0.25	0.39	0.40
Zr	156.56	147.36	181.37	177.04
Y	20.29	24.22	21.77	23.57
Pb	0.58	0.33	0.69	0.00
La	18.54	20.60	16.86	15.55
Ce	39.31	43.69	37.06	34.85
Pr	5.24	5.74	5.14	4.85
Nd	22.23	25.10	23.04	23.56
Sm	5.09	5.71	5.68	5.53
Eu	1.77	1.88	1.88	1.84
Gd	5.16	5.77	6.26	5.94
Tb	0.75	0.96	0.86	0.84
Dy	4.32	4.70	5.07	4.98
Ho	0.81	0.93	0.80	0.93
Er	1.92	2.37	2.15	2.40
Tm	0.26	0.35	0.30	0.31
Yb	1.54	2.07	1.68	1.82
Lu	0.23	0.28	0.24	0.25

Table 6. Main parameters used in the OBS1 model (Kimura and Kawabata, 2015).

Parameter	Value
Primary melts	Robinson Crusoe (Alpha): LL040213-2 (most representative) LL250711-7 (relatively low La/Yb) Alejandro Selkirk (O'Higgins): MF-3 (most representative) MF-6 (relatively low La/Yb)
Melting model	Metasomatic
DM composition	Workman and Hart, 2005
Pyroxenite comp.	Pearce and Parkinson, 1993 (N-MORB)
Enriched peridotite comp.	Sun and McDonough, 1989
Additional DM depletion	0%
H ₂ O in the source	0.03 wt%
Fitting window	15% (Nb/Zr, La/Yb, Nb, Zr, La, Yb) 30% (Nd, Sm, Hf, Eu, Gd, Tb, Dy, Y, Ho, Er, Tm, Lu) 60% (Ta, Ce, Pr, Sr) 200% (Th)

Table 7. Results of the OBS1 model (Kimura and Kawabata, 2015) for samples from the Robinson Crusoe and Alejandro Selkirk Islands, volcanoes representative of the shield-stage in the JFR. The main parameters shown are pyroxenite fraction (Px_{fr}), potential temperature (T_p), pressure at melting termination (P_{mt}), and degree of melting at melting termination (for pyroxenite, PxF_{mt} ; metasomatized peridotite, $PerF_{mt}$; and total, $TotF_{mt}$).

Sample	Px_{fr} (w/f)	T_p (°C)	P_{mt} (GPa)	$TotF_{mt}$ (wt%)	$PerF_{mt}$ (wt%)	PxF_{mt} (wt%)
<i>Robinson Crusoe Island</i>						
LL040213-2 (min-max)	0.6 – 8.8	1316 – 1366	2.42 – 2.68	3.4 – 7.4	1.3 – 4.0	33.8 – 53.9
(mean)	5.0	1341	2.55	4.7	2.5	44.7
L250711-7	0.4 – 6.4	1312 – 1340	2.30 – 2.52	2.4 – 4.8	1.7 – 3.2	35.3 – 46.6
	3.0	1325	2.43	3.6	2.5	40.1
<i>Alejandro Selkirk Island</i>						
MF-3	6.0 – 18.4	1334 – 1412	2.38 – 2.74	7.2 – 19.2	2.5 – 7.5	42.4 – 66.2
	12.0	1371	2.56	11.2	4.6	54.9
MF-6	4.2 – 14.0	1322 – 1386	2.30 – 2.62	5.6 – 14.1	2.2 – 6.0	38.1 – 61.4
	9.3	1356	2.47	8.8	4.0	50.9

Figure 1. Bathymetric map of the JFR and the seafloor around it (GEBCO, SHOA and data from Astudillo, 2014). The O'Higgins Guyot, Alpha Seamount, Robinson Crusoe Island, Santa Clara Island, and Alejandro Selkirk Island, the main volcanoes of the JFR, are shown with their shield-stage $^{40}\text{Ar}/^{39}\text{Ar}$ ages (Lara et al., 2018b). The inset shows the locations of major oceanic bathymetric features and islands (Eas: Easter, SyG: Salas y Gomez, SF-SA: San Félix and San Ambrosio) around the JFR.

Figure 2. Plots of Mg number (Mg#) vs. the contents of major ($\text{CaO}/\text{Al}_2\text{O}_3$) and trace elements (Sc, Ni, and Sr in ppm) for lavas from the shield-stage of O'Higgins Guyot, Alpha Seamount, Robinson Crusoe Island, and Alejandro Selkirk Island. The dashed lines in the Ni plots mark the boundaries between compositional groups defined in Reyes et al. (2017).

Figure 3. Total alkali vs. silica classification diagram for lavas and dykes from the shield-building stage in O'Higgins Guyot, Alpha Seamount, Robinson Crusoe Island, and Alejandro Selkirk Island (after Le Maitre, 2002). The field of alkaline JFR rejuvenated lavas (from O'Higgins Guyot and Robinson Crusoe Island) is also shown. Published data from Reyes et al. (2017) and Lara et al. (2018a) are also included. Figure S.1 shows that Na and K were not substantially mobilized in the JFR shield lavas, allowing the use of the TAS diagram.

Figure 4. Plots showing the variation in trace element content based on new ICP-MS data for lavas from the shield-stage of O'Higgins Guyot, Alpha Seamount, Robinson Crusoe Island, and Alejandro Selkirk Island. Incompatible element enrichment is evident for the Robinson Crusoe and Alpha samples, as reflected by the higher values of Nb/Zr (0.16) compared to in the Alejandro Selkirk/O'Higgins samples (0.11). In contrast, La/Yb does not vary significantly. The plots of Ti/Ti^* vs. Nb/Nb^* and Gd/Yb vs. Ta/Ta^* provide evidence for a moderate 'TITAN' anomaly (calculated according to Peters and Day, 2014) and similar values of HREE slope (Gd/Yb) in JFR volcanoes. The enrichments in Ti, Nb, and Ta vs. Mg# are also shown to demonstrate that fractional crystallization cannot explain the origin of the 'TITAN' anomalies.

Figure 5. Diagrams showing the isotopic variation in the shield-stage lavas of the JFR: (a) $^{206}\text{Pb}/^{204}\text{Pb}$ vs. $^{207}\text{Pb}/^{204}\text{Pb}$ and $^{208}\text{Pb}/^{204}\text{Pb}$ and (b) $^{87}\text{Sr}/^{86}\text{Sr}$ vs. $^{143}\text{Nd}/^{144}\text{Nd}$. The values are characteristic of a FOZO component. Our Pb isotope data and especially $^{207}\text{Pb}/^{204}\text{Pb}$ show significantly lower variation than some published data, suggesting the within-run fractionation of Pb isotopes during analyses. The published JFR data are from Gerlach et

al. (1986), Baker et al. (1987), and Truong et al. (2018). Isotopic data (from GEOROC database) of sites representative of mantle end-member compositions are also shown: HIMU (St Helena, Mangaia and Tubuai), EM1 (Pitcairn and Walvis Ridge) and EM2 (Samoa and Society).

Figure 6. Plots of Mg number (Mg#) vs. $\text{CaO}/\text{Al}_2\text{O}_3$, La/Yb, La, and Yb for shield lavas from Robinson Crusoe and Alejandro Selkirk Islands. Stars indicate the primary melts according to the PRIMACALC2 model (Kimura and Ariskin, 2014) applied to parental samples, and curves show the results of COMAGMAT 3.72 model (Ariskin and Barmina, 2004) for fractional crystallization (2 kbar, 0.8 wt% H_2O , QFM buffer; details in the text). Yellow represents the most representative sample in each case. Black represents a small group of samples with relatively low La/Yb (with respect to the main values).

Figure 7. Geochemical evidence of pyroxenite involvement in the source of the JFR shield-stage. Only 'near-primitive' samples are plotted to exclude the effects of fractionation and accumulation. (a) Plots of MgO (wt%) vs. CaO (wt%), which shows low CaO content for a given MgO in the field of pyroxenite partial melts (only tholeiitic samples, no clinopyroxene or plagioclase on the liquid line of descent; according to Herzberg, 2006). (b) Plots of TiO_2 (wt%) vs. FC3MS ($\text{FeO}/\text{CaO}-3\text{MgO}/\text{SiO}_2$) show values near those of pyroxenite melts with an average value of 0.46. Some values are above the maximum value of FC3MS (0.65) for peridotite melts (average values from Yang and Zhou, 2013). The high values of TiO_2 with respect to EPR (MORB) suggest that the JFR lava source contains more pyroxenite than the EPR lava source (Prytulak and Elliot, 2007). (c) Plots of MnO (wt%) vs. Fe/Mn indicate that the JFR lavas plot in the field of pyroxenite partial melt (high content of Fe/Mn at a given MnO, based on Liu et al., 2008 and Hoang et al., 2018).

Figure 8. OBS1 model results for the most representative samples for Robinson Crusoe (LL040213-2, squares) and Alejandro Selkirk (MF-3; triangles) volcanoes for different water contents in the mantle source (0, 0.03, and 0.06 wt%). Average (large marks) along with maximum and minimum (small marks) results are shown for each water content in the mantle source.

Figure 9. Primitive mantle-normalized (PM from Sun and McDonough, 1989) patterns for the trace-element contents of primitive melts (modeled from parental samples) for the Robinson Crusoe and Alejandro Selkirk volcanoes (red and green, respectively). The black patterns represent the maximum, average, and minimum trace-element contents of the

melts generated by OBS1 (metasomatic mode, 0.03 wt% H₂O in the mantle source; Kimura and Kawabata, 2015) compared with the targets (primary melts) to evaluate the proposed model. The more pyroxenitic signature of the Robinson Crusoe lavas (compared to Alejandro Selkirk) is demonstrated by the values of some incompatible elements (e.g., Ta, Nb, and HREEs). The average values of potential temperature (T_p), pressure at melting termination (P_{mt}), pyroxenite fraction (Px_{fr}) and degree of melting at melting termination (for pyroxenite, PxF_{mb} ; metasomatized peridotite, $PerF_{mb}$; and total, $TotF_{mt}$) that satisfy the model conditions are also shown. A good fit is visible for most of the analyzed elements, and only some elements (e.g., Pr, Sr, and Hf) are slightly different than those calculated by the model (details in the text). n indicates the number of successful OBS1 successful results.

Supplementary data

Table S.1. Major- and trace-element contents of the expected and measured standards used in Acme Labs.

Table S.2. Major- and trace-element contents of whole-rock samples from this study and their duplicates.

Table S.3. Details of the main results obtained from the OBS1 model (Kimura and Kawabata, 2015) using the metasomatic model and 0.03 wt% H₂O in the mantle source.

Figure S.1. Plots of the contents of mobile elements [Na₂O and K₂O (wt%) and U (ppm)] vs. an immobile element (Nb) for lavas from O'Higgins Guyot, Alpha Seamount, Robinson Crusoe Island, and Alejandro Selkirk Island. The correlations indicate that even though low-temperature alteration may have affected the mobile elements (Na, K, and U), they can still be used with caution for petrogenetic interpretations (e.g., TAS diagram).

Figure S.2. Plots of Mg number (Mg#) vs. major elements (Fe₂O₃^T, TiO₂, Na₂O, Al₂O₃, K₂O, and P₂O₅) for JFR shield-stage lavas.

Figure S.3. Primitive mantle-normalized (PM from Sun and McDonough, 1989) patterns showing the abundance of incompatible elements for samples from the O'Higgins (yellow), Alpha (blue), Robinson Crusoe (red), and Alejandro Selkirk (green) volcanoes. The data reveal the relative chemical enrichment of Robinson Crusoe/Alpha samples with respect to Alejandro Selkirk/O'Higgins samples.

Figure S.4. Primitive mantle-normalized (PM from Sun and McDonough, 1989) patterns showing the trace-element contents of primitive melts from the Robinson Crusoe and Alejandro Selkirk Islands (red and green, respectively). Samples LL250711-7 and MF-6 represent a few samples with relatively low ratios of La/Yb and were modeled in OBS1 to evaluate the proposed model. See Figure 9 in the main text for details.

Figure 1. Bathymetric map of the JFR and the seafloor around it (GEBCO, SHOA and data from Astudillo, 2014). The O'Higgins Guyot, Alpha Seamount, Robinson Crusoe Island, Santa Clara Island, and Alejandro Selkirk Island, the main volcanoes of the JFR, are shown with their shield-stage $^{40}\text{Ar}/^{39}\text{Ar}$ ages (Lara et al., 2018b). The inset shows the locations of major oceanic bathymetric features and islands (Eas: Easter, SyG: Salas y Gomez, SF-SA: San Félix and San Ambrosio) around the JFR.

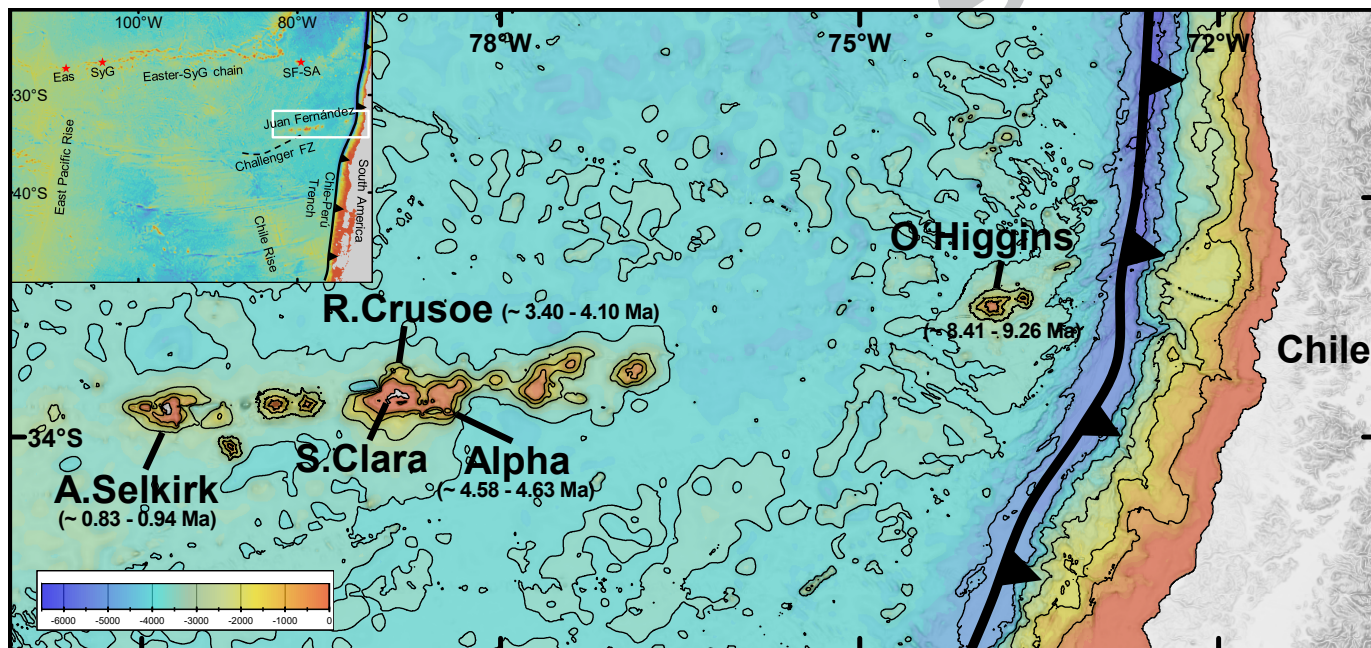


Figure 2. Plots of Mg number (Mg#) vs. the contents of major ($\text{CaO}/\text{Al}_2\text{O}_3$) and trace elements (Sc, Ni, and Sr in ppm) for lavas from the shield-stage of O'Higgins Guyot, Alpha Seamount, Robinson Crusoe Island, and Alejandro Selkirk Island. The dashed lines in the Ni plots mark the boundaries between compositional groups defined in Reyes et al. (2017).

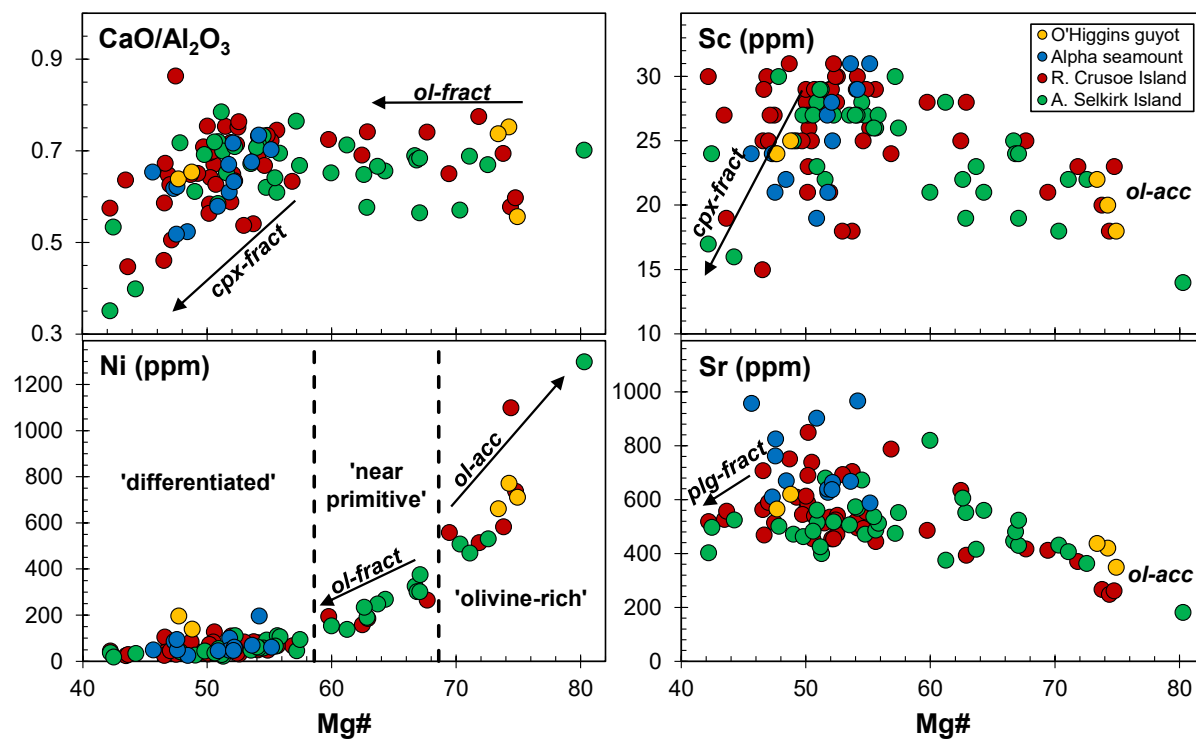


Figure 3. Total alkali vs. silica classification diagram for lavas and dykes from the shield-building stage in O'Higgins Guyot, Alpha Seamount, Robinson Crusoe Island, and Alejandro Selkirk Island (after Le Maitre, 2002). The field of alkaline JFR rejuvenated lavas (from O'Higgins Guyot and Robinson Crusoe Island) is also shown. Published data from Reyes et al. (2017) and Lara et al. (2018a) are also included. Figure S.1 shows that Na and K were not substantially mobilized in the JFR shield lavas, allowing the use of the TAS diagram.

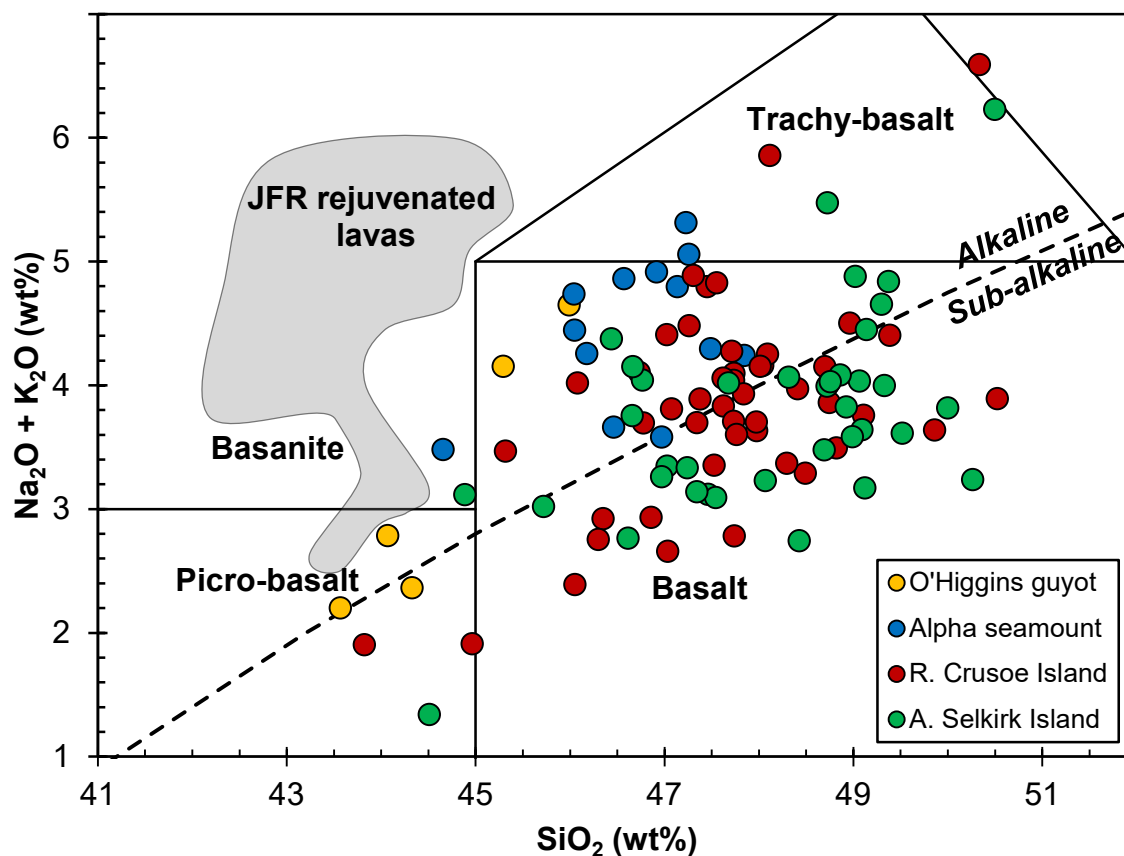


Figure 4. Plots showing the variation in trace element content based on new ICP-MS data for lavas from the shield-stage of O'Higgins Guyot, Alpha Seamount, Robinson Crusoe Island, and Alejandro Selkirk Island. Incompatible element enrichment is evident for the Robinson Crusoe and Alpha samples, as reflected by the higher values of Nb/Zr (0.16) compared to in the Alejandro Selkirk/O'Higgins samples (0.11). In contrast, La/Yb does not vary significantly. The plots of Ti/Ti* vs. Nb/Nb* and Gd/Yb vs. Ta/Ta* provide evidence for a moderate 'TITAN' anomaly (calculated according to Peters and Day, 2014) and similar values of HREE slope (Gd/Yb) in JFR volcanoes. The enrichments in Ti, Nb, and Ta vs. Mg# are also shown to demonstrate that fractional crystallization cannot explain the origin of the 'TITAN' anomalies.

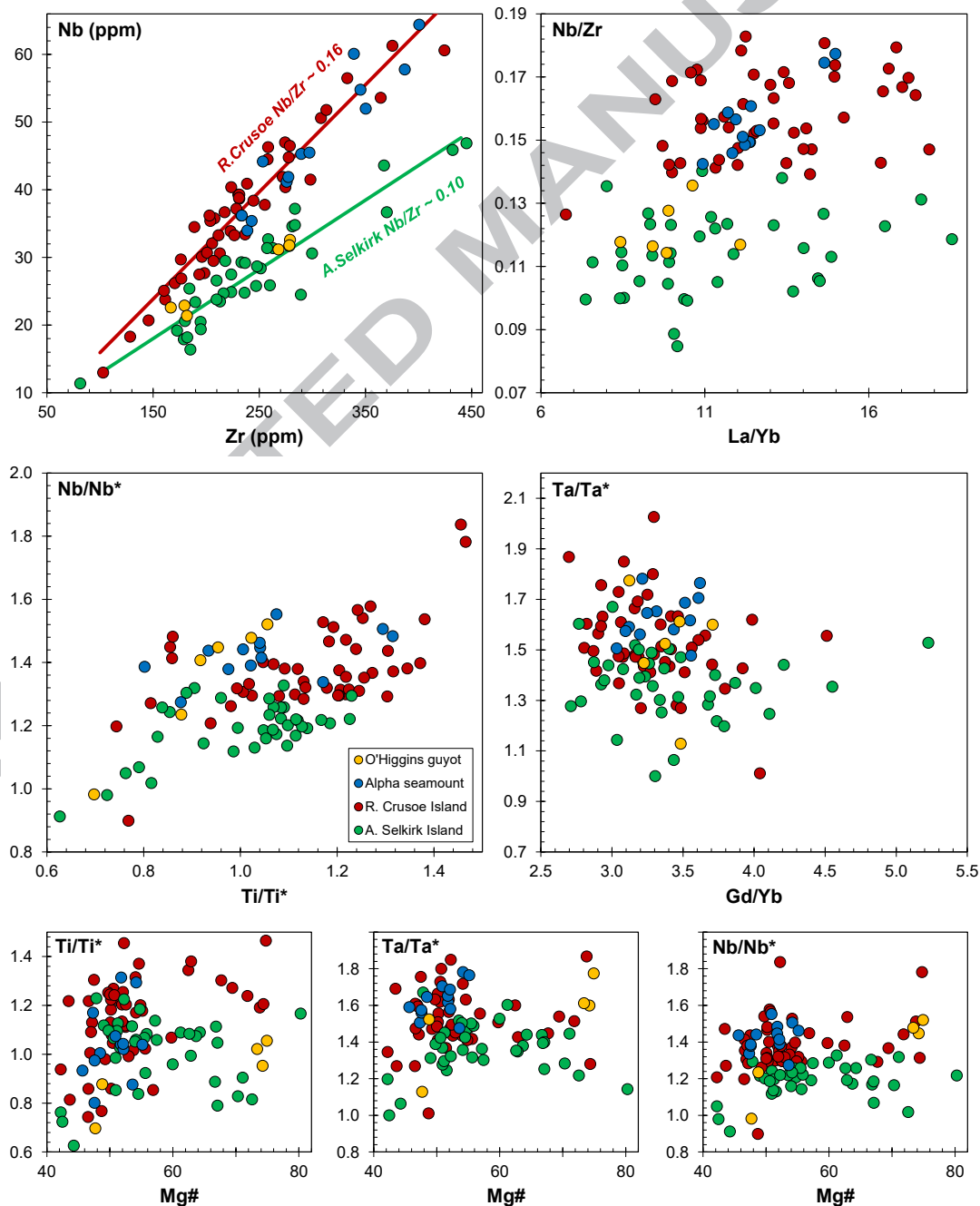


Figure 5. Diagrams showing the isotopic variation in the shield-stage lavas of the JFR: (a) $^{206}\text{Pb}/^{204}\text{Pb}$ vs. $^{207}\text{Pb}/^{204}\text{Pb}$ and $^{208}\text{Pb}/^{204}\text{Pb}$ and (b) $^{87}\text{Sr}/^{86}\text{Sr}$ vs. $^{143}\text{Nd}/^{144}\text{Nd}$. The values are characteristic of a FOZO component. Our Pb isotope data and especially $^{207}\text{Pb}/^{204}\text{Pb}$ show significantly lower variation than some published data, suggesting the within-run fractionation of Pb isotopes during analyses. The published JFR data are from Gerlach et al. (1986), Baker et al. (1987), and Truong et al. (2018). Isotopic data (from GEOROC database) of sites representative of mantle end-member compositions are also shown: HIMU (St Helena, Mangaia and Tubuai), EM1 (Pitcairn and Walvis Ridge) and EM2 (Samoa and Society).

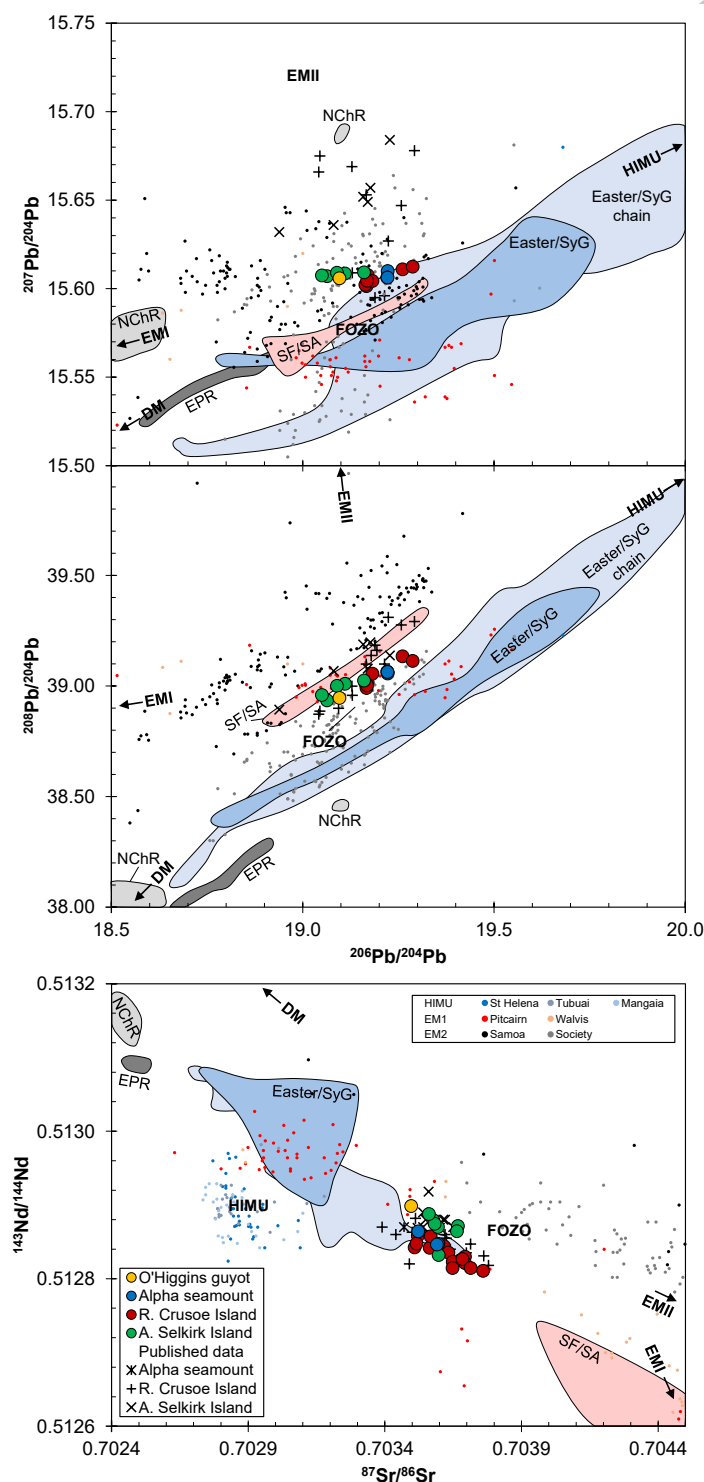


Figure 6. Plots of Mg number (Mg#) vs. $\text{CaO}/\text{Al}_2\text{O}_3$, La/Yb , La, and Yb for shield lavas from Robinson Crusoe and Alejandro Selkirk Islands. Stars indicate the primary melts according to the PRIMACALC2 model (Kimura and Ariskin, 2014) applied to parental samples, and curves show the results of COMAGMAT 3.72 model (Ariskin and Barmina, 2004) for fractional crystallization (2 kbar, 0.8 wt% H_2O , QFM buffer; details in the text). Yellow represents the most representative sample in each case. Black represents a small group of samples with relatively low La/Yb (with respect to the main values).

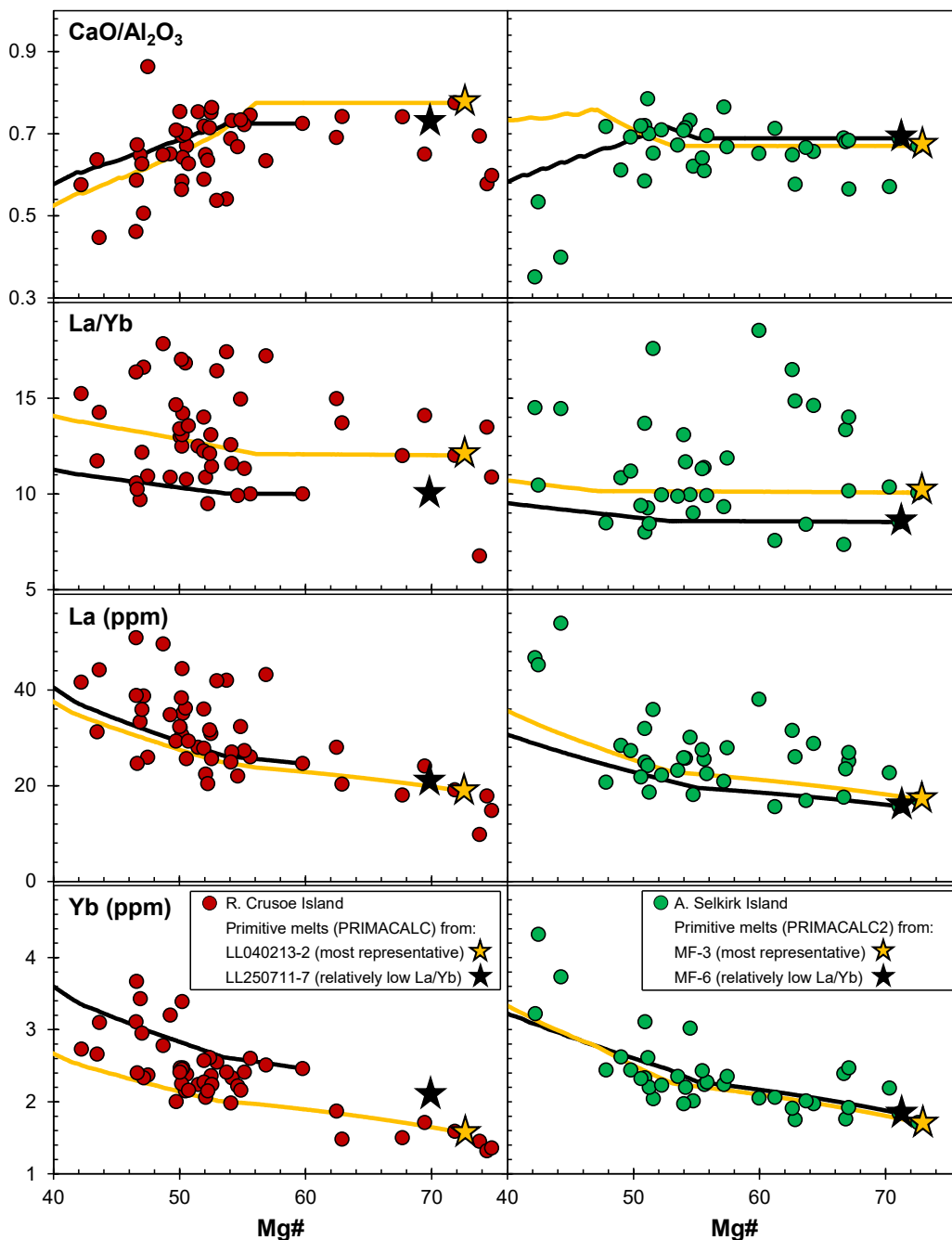


Figure 7. Geochemical evidence of pyroxenite involvement in the source of the JFR shield-stage. Only ‘near-primitive’ samples are plotted to exclude the effects of fractionation and accumulation. (a) Plots of MgO (wt%) vs. CaO (wt%), which shows low CaO content for a given MgO in the field of pyroxenite partial melts (only tholeiitic samples, no clinopyroxene or plagioclase on the liquid line of descent; according to Herzberg, 2006). (b) Plots of TiO_2 (wt%) vs. FC3MS ($\text{FeO}/\text{CaO}-3\text{MgO}/\text{SiO}_2$) show values near those of pyroxenite melts with an average value of 0.46. Some values are above the maximum value of FC3MS (0.65) for peridotite melts (average values from Yang and Zhou, 2013). The high values of TiO_2 with respect to EPR (MORB) suggest that the JFR lava source contains more pyroxenite than the EPR lava source (Prytulak and Elliot, 2007). (c) Plots of MnO (wt%) vs. Fe/Mn indicate that the JFR lavas plot in the field of pyroxenite partial melt (high content of Fe/Mn at a given MnO, based on Liu et al., 2008 and Hoang et al., 2018).

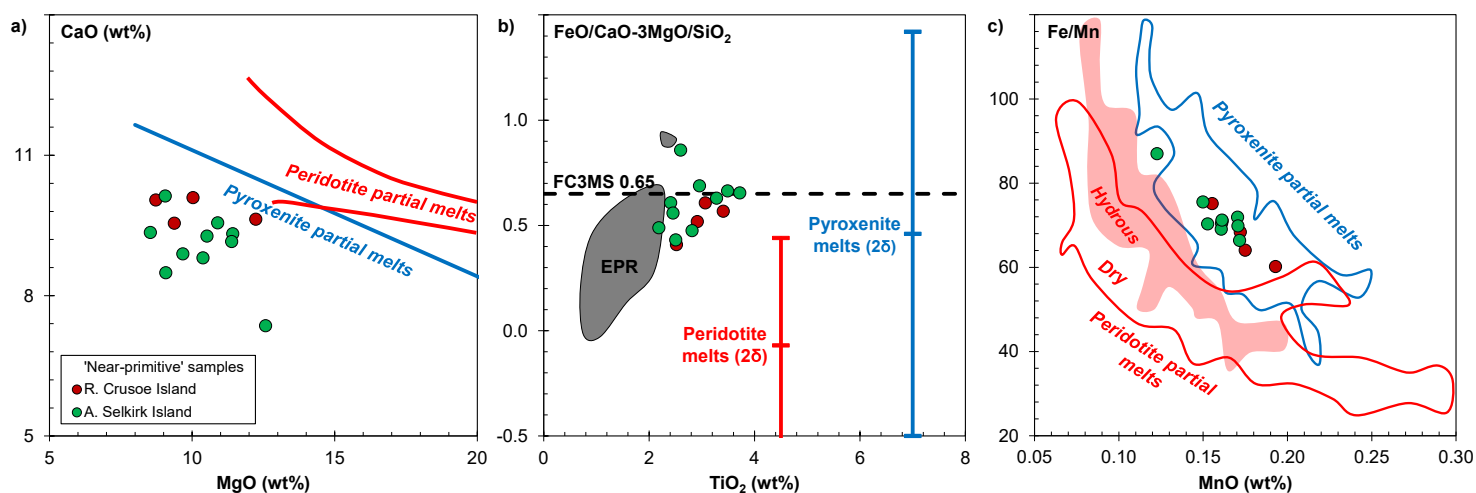


Figure 8. OBS1 model results for the most representative samples for Robinson Crusoe (LL040213-2, squares) and Alejandro Selkirk (MF-3; triangles) volcanoes for different water contents in the mantle source (0, 0.03, and 0.06 wt%). Average (large marks) along with maximum and minimum (small marks) results are shown for each water content in the mantle source.

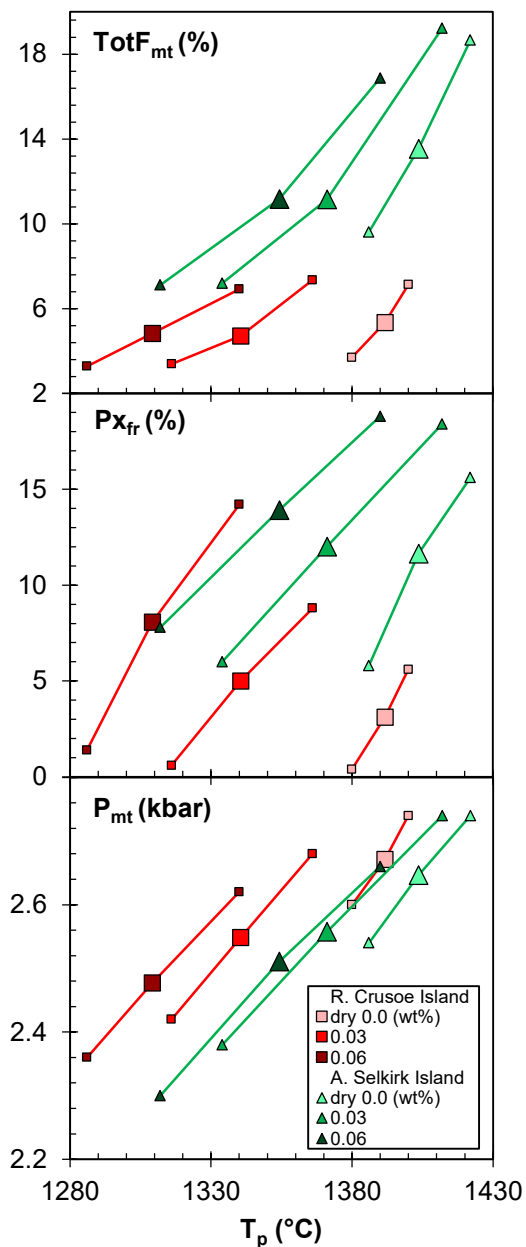


Figure 9. Primitive mantle-normalized (PM from Sun and McDonough, 1989) patterns for the trace-element contents of primitive melts (modeled from parental samples) for the Robinson Crusoe and Alejandro Selkirk volcanoes (red and green, respectively). The black patterns represent the maximum, average, and minimum trace-element contents of the melts generated by OBS1 (metasomatic mode, 0.03 wt% H₂O in the mantle source; Kimura and Kawabata, 2015) compared with the targets (primary melts) to evaluate the proposed model. The more pyroxenitic signature of the Robinson Crusoe lavas (compared to Alejandro Selkirk) is demonstrated by the values of some incompatible elements (e.g., Ta, Nb, and HREEs). The average values of potential temperature (T_p), pressure at melting termination (P_{mt}), pyroxenite fraction (Px_{fr}) and degree of melting at melting termination (for pyroxenite, PxF_{mt} ; metasomatized peridotite, $PerF_{mt}$; and total, $TotF_{mt}$) that satisfy the model conditions are also shown. A good fit is visible for most of the analyzed elements, and only some elements (e.g., Pr, Sr, and Hf) are slightly different than those calculated by the model (details in the text). n indicates the number of successful OBS1 successful results.

